

1 Chemical sparsity in Bayesian receptor models for aerosol 2 source apportionment

3 Marta Via¹, Jure Demšar², Yufang Hao³, Manousos Manousakas^{3,4}, Anton Rusanen⁵, Jianhui
4 Jiang⁶, Stuart K. Grange⁷, Jean-Luc Jaffrezo⁸, Vy Ngoc Thuy Dinh⁸, Gaëlle Uzu⁸, Griša
5 Močnik¹, and Kaspar R. Daellenbach³

6
7 ¹Center for Atmospheric Research, University of Nova Gorica, Ajdovščina 5270, Slovenia

8 ²Faculty of Computer and Information Science, Večna pot 113, 1000 Ljubljana, Slovenia

9 ³Laboratory of Atmospheric Chemistry, Paul Scherrer Institute, 5232 Villigen PSI, Switzerland

10 ⁴Environmental Radioactivity Aerosol Tech. for Atmospheric Climate Impacts, INRaSTES, National Centre of
11 Scientific Research “Demokritos”, Ag. Paraskevi, 15310, Greece

12 ⁵Atmospheric Composition Research, Finnish Meteorological Institute, 00101 Helsinki, Finland

13 ⁶School of Ecological and Environmental Sciences, East China Normal University, 200241, Shanghai, China

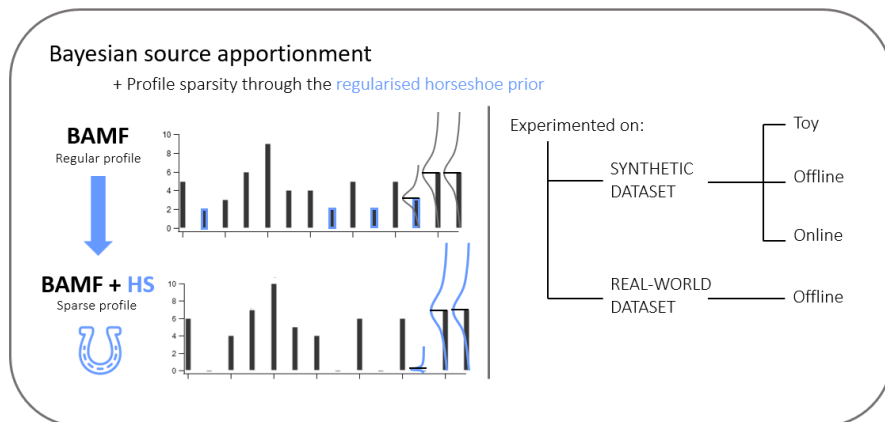
14 ⁷Climate and Environmental Physics, Physics Institute, University of Bern, Sidlerstrasse 5, 3012 Bern,
15 Switzerland

16 ⁸University of Grenoble Alpes, CNRS, INRAE, IRD, Grenoble INP, IGE, Grenoble 38000, France

17
18 *Correspondence to:* Marta Via (marta.viagonzalez@ung.si) and Kaspar R. Daellenbach
19 (kaspar.daellenbach@psi.ch)

Field Code Changed

20 **Abstract.** Aerosol source apportionment is a key tool for understanding the origins of atmospheric particulate
21 matter and for guiding effective air quality management strategies. However, source apportionment techniques
22 still struggle to properly separate highly correlated sources without relying on restrictive *a priori* information,
23 possibly skewing the solution and adding subjective operator input, with varying degrees of benefit. This study
24 introduces sparsity into the Bayesian Autocorrelated Matrix Factorisation (BAMF) model with the aim of
25 removing non-essential species contribution in the unconstrained profiles, which is expected to improve the
26 separation of factors compared to BAMF. The regularised horseshoe prior (HS) has been added to BAMF
27 (BAMF+HS) to promote composition matrix \mathbf{F} sparsity, shrinking low-signal contributions to the solutions.
28 BAMF+HS was evaluated using three synthetic datasets designed to reflect increasing levels of data complexity
29 (Toy, representing a highly simplified dataset; Offline, representing a filter dataset; and Online, representing an
30 Aerosol Chemical Speciation Monitor (ACSM)-like dataset), and a real-world multi-site filter dataset. The results
31 demonstrate that BAMF+HS effectively enforces sparsity in offline datasets and that this improves accuracy in
32 reconstructing source profiles and time series compared to BAMF and Positive Matrix Factorisation (PMF).
33 However, its application to higher-complexity ACSM datasets revealed sensitivity to sampling instability
34 hindering sparsification. With that, even though sparsity was not achieved, the quality of the BAMF+HS solution
35 metrics were not deprecated compared to BAMF. Overall, this work underscores the value of incorporating profile
36 sparsity as a solution property in Bayesian source apportionment, and positions BAMF+HS as a promising model
37 for source apportionment.



39

40 **1. Introduction**

41 Particulate Matter (PM) adversely affects human health through both short and sustained exposures (Pope and
 42 Dockerty, 1999, Yang et al. 2019). The observed relationship between decreasing PM concentrations and
 43 increased life expectancy (Keuken et al. 2011; Zheng et al. 2022) highlights the importance of developing
 44 mitigation plans grounded in detailed knowledge of PM sources composition and concentrations. Moreover,
 45 because some proxies for aerosol toxicity, among them oxidative potential, are highly dependent on its sources
 46 (Daellenbach et al. 2020), implementing source-specific mitigation measures contributes to more quantitative and
 47 efficient abatement and a more effective protection of the population.

48
 49 Source apportionment is the process of identifying and quantifying sources by using information about their
 50 chemical composition, and is commonly conducted through receptor models (RMs) which differentiate PM
 51 sources according to the distinctness of their chemical composition and time series characteristics. The most
 52 widely used RM is the Positive Matrix Factorisation model (PMF, Paatero and Tapper, 1994), which deconvolutes
 53 the input chemical composition into the product of composition and time series matrices (**F** and **G**, respectively),
 54 and minimises the residuals of the fit through the weighted least squares loss. The factorisation equation, hence,
 55 is written as

$$56 \quad X = G \cdot F + E, \quad (1)$$

57 where **X** is the input matrix, a $n \cdot m$ matrix of n timepoints and m species, which is decomposed into **G** and **F**,
 58 matrices of dimensions $n \cdot p$ and $p \cdot m$, respectively, where p is the number of factors, and **E** is the residuals matrix
 59 of dimensions $n \cdot m$.

60
 61 Unconstrained PMF, although it can lead to robust results, is usually insufficient when the sources are highly
 62 correlated or have very similar source profiles. In such cases, guiding the model by introducing a priori knowledge
 63 (common practice known as constraining the model) has been proven beneficial for the source deconvolution
 64 (Lingwall and Christensen et al. 2007, Belis et al. 2014, Dinh et al. 2025). However, it can still introduce

65 substantial bias in the solution (Via et al. 2022). Globally, the RMs cover the whole range of pollution sources
66 knowledge required prior to receptor modelling (Viana et al. 2008, Belis et al. 2013). A very strongly-constrained
67 RM is the Chemical Mass Balance model (CMB), which factorises the initial matrices with a totally fixed \mathbf{G} or \mathbf{F} .
68

69 Bayesian models represent a probabilistic alternative to the PMF framework. The first application of Bayesian
70 models in atmospheric source apportionment was introduced in Park et al. (2001, 2002) for Volatile Organic
71 Compounds (VOC) source apportionment. In this approach, the mass closure condition was taken to the Bayesian
72 framework and an autocorrelation prior, AR(1) (the first order autoregression formulation), was applied,
73 improving the solution given assuming independent \mathbf{G} components. The autocorrelation prior importance was
74 later reinforced in Rusanen et al. (2024) with a differently formulated autocorrelation prior. The latter shows the
75 added value of the Bayesian Autocorrelated Matrix Factorisation model (BAMF) in-comparison-to-PMF-in
76 different-kinds-of-compared-with-PMF-across-different spectrometry-based PM synthetic datasets. The Bayesian
77 Multivariate receptor modelling software BNFA and bayesMRM (Park and Oh, 2021) were developed to provide
78 user-friendly tools for Bayesian source apportionment.

79
80 However, studies using the Bayesian Matrix Factorisation framework are still scarce. Some examples are Oh and
81 Park (2022), which employed a Bayesian RM to conduct multi-site source apportionment, and Zhang et al. (2023),
82 which performed NH_4^+ source apportionment through the Bayesian SIMMR package (Govan et al. 2023).
83 Bayesian models have also been used as a complement to standard RMs, as in Balachandran et al. (2013) where
84 a Bayesian model processing ensemble solutions of a chemical transport model and solutions of three RMs are
85 produced to then use it in CMB for production of final results. The Bayesian model focused on attributing the
86 proper weight to each of the ensemble components and improved the correlation of sources with their markers
87 compared to the traditional approach. Bayesian inference has also been used in Park et al. (2002) and Dai et al.
88 (2024) to generate spatially resolved source apportionment solutions adjusting the weights of each location
89 solution in a multi-site data scheme.

90
91 Thus, Bayesian Matrix Factorisation has become an effective and powerful tool for aerosol source apportionment.
92 However, to the authors knowledge, little attention has been given to improving the accuracy of chemical
93 composition profiles, i.e. \mathbf{F} components. This highlights the fundamental challenge in receptor modelling of
94 obtaining chemically distinct and interpretable source profiles from complex and mixed emission sources.
95 Moreover, it has been shown in Rusanen et al. (2024) that in BAMF, slight differences of \mathbf{F} can severely
96 compromise the quality of \mathbf{G} (Figure S2 in the mentioned article), hence, steps towards \mathbf{F} refining should result
97 in overall source apportionment method improvement. In this context, sparsity, defined as the property of a
98 dataset, model or solution in which only a limited number of elements are substantial contributions while most
99 are zero or close to zero, could be favourable for this problem. The accomplishment of sparse source fingerprints
100 could represent “cleaner” emission sources with less mixing among resolved factor profiles, since substituting
101 non-significant contributions in a factor by zeros might allow allocating more importance to the actually relevant
102 contributions of species in factors. This work aims to implement sparsity on chemical fingerprints in BAMF
103 aiming for a more accurate source apportionment. We introduce sparsity with the regularised horseshoe prior
104 (Piironen and Vehtari, 2017), which unlike other sparsity priors, enables regularisation of the sparsity strength,

105 and compare it with other sparsity priors, such as Lasso (Tibshirani et al. 2015) and Spike-and-slab (Andersen et
106 al. 2014). This model is then tested on three synthetic datasets with different complexity degrees and one real-
107 world dataset to depict the impact of sparsity and potential benefits of its implementation.

108 2. Methodology

109 2.1 Bayesian Matrix Factorisation

110 Bayesian Matrix factorisation models, like other RMs, are based on the chemical mass balance equation (Eq. 1).
111 Bayesian modeling approaches this problem probabilistically and bases the determination of the matrices, \mathbf{F} and
112 \mathbf{G} , the main parameters to determine, upon the assumptions imposed on the model, i.e. priors. Bayesian
113 factorisation forces the decomposition through modelling the \mathbf{X} matrix components as a Gaussian with center on
114 the “noise-free data matrix” \mathbf{Z} (matrix of dimensions $n \cdot m$) and a standard deviation given by the positively-defined
115 uncertainty matrix (Eq. 2). The matrix σ (positive matrix of dimensions $n \cdot m$) represents the uncertainties of the
116 measurements. The matrix \mathbf{Z} is, in turn, the product of the time series and profiles submatrices, \mathbf{G} and \mathbf{F} ,
117 respectively, and (a) is rewritten as:

$$118 X \sim N(\mathbf{Z}, \sigma) = N(\mathbf{G} \cdot \mathbf{F}, \sigma) \quad (2)$$

120 where N represents the normal distribution. With that formulation, the measurements matrix \mathbf{X} is modeled into a
121 Gaussian distribution whose centre is the $\mathbf{G} \cdot \mathbf{F}$ product matrix and its standard deviation is the uncertainty matrix
122 σ . In turn, one introduces certain restrictions on the \mathbf{F} , \mathbf{G} , matrices characteristics in the form of priors. Whilst \mathbf{G}
123 is not given any prior and is sampled then by default from a uniform distribution, \mathbf{F} is modelled as a Dirichlet
124 distribution to ensure positivity, with the sum of its components being equal to 1 (2):

$$125 F_k \sim \text{Dirichlet}(1_m) \quad (3)$$

126 With these \mathbf{F} requirements, profiles represent the normalised contribution to the spectra of one source. Usual
127 notation for indices used hereinafter are i, j, k for elements in the range $(1, \dots, n)$, $(1, \dots, m)$, and $(1, \dots, p)$, for the
128 timestamps, species, and factors, respectively. It is worth noting that PMF applies the normalisation of profiles
129 after a \mathbf{F} , \mathbf{G} solution is found, not as a model prior as done in BAMF. The PMF generates mass-loaded \mathbf{F} , \mathbf{G}
130 solution matrices, which are reweighted to provide a normalised \mathbf{F} and a mass-loaded \mathbf{G} . In the Bayesian models
131 used in this study, the normalisation of \mathbf{F} is inherent to the model by design. The different formulations eventually
132 provide normalised \mathbf{F} and mass-weighted \mathbf{G} , with unlikely affectations due to the normalisation procedure. The
133 model configuration given by (2) and (3) will be referred to as Bayesian Factorisation model (BMF) and represents
134 the analog of PMF in the Bayesian framework. All models used in this manuscript are outlined in Table 1.

135
136 On top of this structure, Rusanen et al (2024) proposed an autocorrelation prior for \mathbf{G} which should account for
137 the inherent autocorrelation of air pollutant sources in time. The imposition of autocorrelation in \mathbf{G} entails that
138 two consecutive measurements should be more similar than two measurements apart in time, and that the similarity
139 should fade with the temporal gap between them. This property is particularly advantageous for atmospheric
140 pollution dynamics which, generally, are expected to exhibit temporal smoothness rather than abrupt fluctuations.
141 The formulation of the autocorrelation prior for \mathbf{G} is given by (4) and includes two more modelling parameters, α

Formatted: Font: Bold

Formatted: Font: Bold

Formatted: Font: Not Bold, English (United States)

Formatted: English (United States)

Formatted: Font: Not Bold

Formatted: Font: Bold

Formatted: Font: (Default) Times New Roman, Font color: Auto, English (United States), Pattern: Clear

Formatted: English (United States)

Formatted: Font: (Default) Times New Roman, Font color: Auto, English (United States), Pattern: Clear

142 (positive vector or dimension p) and β (positive vector or dimension p), which regulate the similarity of one \mathbf{G}
 143 component with the previous one as follows:

$$144 \quad G_{i+1,k} \sim C^+(G_{ik}, \alpha_k \cdot \Delta t_i + \beta_k) \quad (4)$$

145 where $i \in (2, \dots, n-1)$, C represents the Cauchy distribution and $+$ represents positive real numbers. This prior
 146 centers the $i+1$ th component distribution in the i th component with a distribution width that linearly depends on
 147 the temporal gap between these two timestamps. Hence, the more temporally-separated two consecutive points
 148 are, the less correlated they are expected to be. The Cauchy distribution was chosen due to its heavier tails which
 149 enable more probable jumps between consecutive i 's than a Gaussian distribution (Gelman et al., 2013). This
 150 flexibility could be convenient for real-world datasets which are affected by measurement gaps. The coefficients
 151 α and β are ~~source-source~~ source-dependent to allow for source-dependent correlation degrees. The model which
 152 introduces this prior to BMF is called Bayesian Autocorrelation Matrix Factorisation model (BAMF, Rusanen et
 153 al. 2024).

154 2.1.1 The horseshoe prior

155 Here we propose a sparsity enforcement into the profiles matrix, intending to remove small contributions of
 156 irrelevant species for a given factor. The introduction of sparsity in BAMF involves the addition of several
 157 hyperpriors in the \mathbf{F} prior to implement the shrinkage mechanism. In this study, we used the regularised horseshoe
 158 prior (Piironen and Vehtari, 2017), which is a global-local complex of hyperpriors, i.e. the shrinkage power is
 159 both regulated globally source-wise and \mathbf{F} -component-wise. The idea behind this prior is that species with very
 160 small contributions to a factor are shrunk toward zero through an automatic shrinkage mechanism, whereas species
 161 with substantial support from the data are largely unaffected. The regularised horseshoe (HS) prior implemented
 162 in \mathbf{F} in the BAMF scheme as

$$163 \quad F_{kj} = \mu_{kj} \cdot \tilde{\lambda}_{kj} \cdot \tau_j, \quad (5)$$

164 where μ (matrix of dimensions $n \cdot m$) represents the \mathbf{F} matrix without the horseshoe prior. μ , in turn is defined as
 165 a standard Cauchy distribution prior as

$$166 \quad \mu_{kj} \sim C^+(0, 1), \quad (6)$$

167 where τ (vector of dimension p) represents the global shrinkage parameters and

$$168 \quad \tau \sim C^+(0, \tau_0 \cdot \sigma_{HS}), \quad (7)$$

169 where the parameter τ_0 can be regulated by the user to regulate the overall shrinkage power and σ_{HS} is sampled
 170 from an uniform distribution. The hyperparameter $\tilde{\lambda}_{kj}$ applies the local shrinkage to

171 as

$$172 \quad \tilde{\lambda}_{kj} = \sqrt{\frac{c^2 \cdot \lambda^2}{c^2 + \lambda^2 \cdot \tau^2}}, \quad (8)$$

173 where

$$174 \quad c^2 \sim \Gamma^{-1}(0.5 \cdot \text{slab_df}, 0.5 \cdot \text{slab_df}) \quad (9)$$

$$175 \quad \lambda \sim \text{slab_scale} \cdot C^+(0, 1) \quad (10)$$

176 both combined providing the characteristic shrinking horseshoe shape. Here, λ is a model parameter of dimensions
 177 $n \cdot m$ which after regularisation becomes is denoted as $\tilde{\lambda}_{kj}$. Further description of the horseshoe implementation
 178 on BAMF can be found in Section S2.1, and the prior derivation and details in Piironen and Vehtari (2018). The
 179 distribution parameters τ_0 , σ_{HS} , and slab_df , slab_scale were tested and results did not show significant sensitivity

180 to their variations, so we keep the default [ones](#) ~~as~~ provided in Piironen and Vehtari (2018) ~~as can be found in~~
181 ~~the~~ available shared codes. The models with the horseshoe (HS) priors are hereinafter marked with "+HS".
182 Figure S1 shows a schematic diagram of the matrix decomposition through BAMF.

183
184 In order to assess the amount of sparsity of a dataset or a solution, we used the Gini coefficient (Gini et al., 1936),
185 which assesses the inequality over a distribution as follows:

$$186 \quad Gini = \frac{\sum_{i=1}^n (2i - n - 1) \cdot x_i}{2 \cdot n \cdot \sum_{i=1}^n x_i} \quad (11)$$

187 where \mathbf{x} values are sorted in ascending order, and n is the number of elements in \mathbf{x} . [It is a proxy for how deviant](#)
188 [a dataset is from the total equality amongst its components](#). Since it quantifies the inequality, it can be a proxy for
189 sparsity; if some values are high and the others are zero, $Gini \approx 1$ ([great inequality](#)), if all values are equal, $Gini$
190 = 0. Also, the solution-to-truth Gini values ratio will be discussed throughout the analysis, referred to as "Gini
191 ratio". To evaluate if the sparsity is enforced precisely where it should, an additional metric has been applied
192 called "zero truth sum". This metric sums up the modelled contributions of the null species in the truth profiles.

193 2.1.2 Alternative factorisation methodologies

194 **BAMF-AR1.** There is an alternative formulation for the autocorrelation prior as introduced in Bayesian models
195 by Park et al. (2001). The AR(1) autocorrelation prior is the first degree polynomial expansion of the
196 autoregressive models and it proposes a linear progression of $G_{i+1,k}$ from $G_{i,k}$. We introduce AR(1) in the Bayesian
197 framework as

$$198 \quad G_{i+1,k} \sim N(\alpha_k \cdot G_{i,k} + \beta_k, \gamma_k) \quad (12)$$

199 In this formulation, the $i+1$ -th point stems from a Gaussian distribution centered linear combination on the i -th
200 point with source-dependent slopes (α) and intercept (β), and width (γ). Although, unlike (4), it disregards the
201 decrease of correlation between gapped consecutive points, this prior allows for source-specific time series trends,
202 which would be beneficial for certain source description. The model which introduces this prior to BMF will be
203 called BAMF-AR1.

204
205 **BAMF-GS.** Another formulation is introduced, switching the Dirichlet distribution to the matrix \mathbf{G} instead of \mathbf{F}
206 (6). This swap should allow \mathbf{F} to retain the \mathbf{X} matrix mass and could potentially help deconvoluting profiles due
207 to the upweighting of the chemical profiles.

$$208 \quad G_k \sim \text{Dirichlet}(1_n) \quad (13)$$

209 Thus, the \mathbf{G} presents two priors, the dirichlet distribution and the autocorrelation prior, whilst \mathbf{F} is sampled from
210 the default uniform distribution. This model will be called hereinafter BAMF-GS as short from BAMF-G simplex,
211 since a simplex is the set of positive vectors that sum to one hence it is the natural geometric structure for the
212 Dirichlet distribution to sit on. This model structure, nevertheless, does not allow for a horseshoe prior application,
213 since due to the factors mass now incorporated in \mathbf{F} , the coefficients will be very distinct from zero and the
214 horseshoe prior will not perceive them as potential signals to sparsify.

215
216 **CMB.** Lastly, a Bayesian formulation of the CMB model was employed in order to test the horseshoe prior
217 capacities with the most proper factorisation possible. This model is mainly analogous to CMB in the Bayesian

218 framework, but the \mathbf{G} matrix was fixed with the truth time series. Hence the model only had to determine the \mathbf{F}
219 components distributions to match the factorisation condition (2) given the truth \mathbf{G} .

220 2.1.3 Solver and Hamiltonian-Monte Carlo Markov Chain

221 All Bayesian models were compiled and run in STAN (Carpenter et al. 2017), a probabilistic programming
222 language developed for Bayesian modelling. STAN solves Bayesian inference through the Hamiltonian Monte
223 Carlo (HMC) algorithm based on Markov Chain Monte Carlo methods (MCMC). HMC uses an approximate
224 Hamiltonian dynamics simulation with the Metropolis acceptance/rejection criterion and a no-U-turn sampler
225 (NUTS, Hoffman and Gelman, 2014). For the sake of brevity, we present only the essential concepts here,
226 directing readers to Carpenter et al. (2017), Gelman et al. (2014), STAN Manual (2025) and references therein for
227 comprehensive information.

228 **The objective of the inference is to retrieve the** parameters of the model, primarily \mathbf{F} and \mathbf{G} but also all the other
229 defined parameters ($\tau, \lambda, \alpha, \beta$). **These** are sampled from their posterior distributions, constructed from the priors
230 and the data introduced. In the Hamiltonian analogy, the evolution of these parameters across samples is computed
231 as the trajectory of a fictitious particle. This particle moves through the parameter space driven by random
232 momentum in all directions. This approach avoids the random-walk behavior of simpler sampling methods and
233 enables faster convergence. The trajectory is hence simulated using a discretized approximation, and candidate
234 positions are accepted or rejected according to the Metropolis criterion (Metropolis et al. 1953). Accepted
235 positions correspond to plausible parameter **values (of the \mathbf{F} , \mathbf{G} , τ , λ , α , and β parameters in our case)** values given
236 both the model assumptions and the data. This process provides a distribution over samples of possible solutions
237 from which confidence intervals of each of the model (hyper)parameters can be extracted. A set of samples is
238 called a chain, each of them initialised with a different seed to explore the solution space more broadly. In order
239 to initialise the model parameters more effectively, the maximum a posteriori (MAP) point parameters solution
240 estimated by STAN is used through the LBFGS algorithm (Liu and Nocedal, 1989). Even if this approach makes
241 the parameter sampling process much more efficient, solutions might have multiple local maxima, and MAP will
242 initialise the models based only on one of those. This highlights the importance of using different seeds to explore
243 the solution space more widely. Since the early iterations of each Markov chain are typically influenced by the
244 starting **values** and may not represent samples from the true posterior distribution, we discarded the first half of
245 the samples from each chain. Different settings were used according to the type of experiment, shown in Table
246 S1. The number of chains is consistent with standard practice in Bayesian modeling, and the number of samples
247 was increased beyond commonly adopted values (e.g., 1000) in order to improve solution stability. As seen in
248 Table S1, the more complex the datasets are, the more time BAMF+HS takes to run. Since the BAMF+HS running
249 times are high at this development stage, BAMF+HS might currently be more adequate for exhaustive source
250 apportionment refinement than real-time monitoring.

251 In order to evaluate the convergence of a solution to the target posterior distribution, the potential scale reduction
252 factor (\hat{R} , Gelman and Rubin, 1992) is used. This coefficient compares the variance within chains and between
253 chains of the Z matrix, hence if chains converge, $\hat{R} \approx 1$, values of $\hat{R} \gg 1$ imply chain divergence and values of $\hat{R} \ll 1$
254 imply sampling divergence in chains. The convergence of all runs has been assessed using standard Bayesian

Formatted: Font: Not Bold

Formatted: Font: Bold

Formatted: English (United States)

Formatted: English (United States)

255 diagnostics, including visual inspection of trace plots, and the effective sample size and \hat{R} statistics, and all
256 experiments shown in the manuscript fall within satisfactory stability ranges for these criteria.

257

258 2.2 PMF

259 In PMF (Paatero and Tapper, 1994), equation (1) is solved through the ME-2 solver (ME2, Paatero, 1999) based
260 on the weighted means squares minimization of the quantity:

$$261 \quad Q = \sum_{j=1}^m \sum_{i=1}^n \left(\frac{e_{ij}}{\sigma_{ij}} \right)^2 \quad (14)$$

262 PMF was implemented on all datasets unconstrainedly through the Source Finder software (SoFi version 9.5,
263 Canonaco et al. 2013) with 100 runs which are posteriorly sorted as in BAMF. The number of runs may seem
264 compromising the PMF quality in comparison to the 4000-12000 samples per chain used in Bayesian models.
265 However, this comparison is misleading, since the factorisation space is indeed better explored by PMF, with 100
266 different sampling seeds, while only 4 seeds (chains) were used in BAMF-like models as usual procedure in
267 Bayesian modelling for the sake of computational resources.

268

269 2.3 Pre- and post- processing for all models

270 Before model running, \mathbf{X} and σ are normalised to use consistent scales of all priors and posteriors for Bayesian
271 models. The normalisation is based on ensuring a mean of $\mathbf{X} = 1$.

$$272 \quad X^* = X / f_{norm} \quad , \quad \sigma^* = \sigma / f_{norm} \quad \text{where} \quad f_{norm} = \sum_{i,j} X_{ij} / (n \cdot m) \quad (15)$$

273 After the factorisation this normalisation is reverted converting the normalised matrices, hereinafter referred as $\bar{\mathbf{G}}$,
274 $\bar{\mathbf{F}}$, to the properly-scaled \mathbf{G} , \mathbf{F} matrices.

275

276 In the model outcomes, the factor ordering in the matrices is random in the model results, hence, the solution
277 factors must be sorted. Here, as in Rusanen et al. (2024), we used the Hungarian algorithm (Kuhn, 1955) to sort
278 the $\bar{\mathbf{Z}}_k$ components ($\bar{\mathbf{Z}}_k = \bar{\mathbf{G}}_{ik} \cdot \bar{\mathbf{F}}_{kj}$, i.e. each factor's normalised \mathbf{Z} submatrix). The metric to sort the components
279 is the Manhattan distance (i.e. the sum of the absolute differences of two Cartesian coordinates). All factors in
280 each chain of samples are then reordered upon the factor order of a small group of samples of that chain (the last
281 5, arbitrarily chosen) and, subsequently, one all-samples-averaged \mathbf{F}_k and \mathbf{G}_k are retrieved for each of the chains.
282 Then, the order of factors of each of the chains is sorted again in the same way in relation to the truth \mathbf{F} , to have
283 all sources equally sorted in all chains. Median and quantiles are computed over samples and chains to produce
284 the final solutions and uncertainties. This sorting process is also used for the PMF solution despite not being its
285 usual sorting approach for the sake of homogeneity in comparison to the Bayesian models.

286

287 The last step of the experimental process was to assess the model performance on the given dataset. The evaluation
288 of the performance should be based on: i. reconstruction performance, or the difference between \mathbf{X} and \mathbf{Z} ; ii.
289 similarity to truth, or environmental sensibility based on the apportionment of source tracers in case the truth is
290 not available; iii. computational performance. The reconstruction performance was assessed by checking the cell-

291 wise correlation between \mathbf{X} and \mathbf{Z} and checking the median and maximum of the absolute value of relative
292 deviations of \mathbf{Z} and \mathbf{X} with respect to the measurement uncertainty matrix σ ($|\mathbf{X}-\mathbf{Z}|/\sigma$). The similarity to truth,
293 when available, is tackled by comparing the median ratio between modelled \mathbf{G} and truth (\mathbf{G}/\mathbf{G}_0), the Pearson
294 correlation for the \mathbf{G} matrix (\mathbf{G}_r), and the Spearman correlation for \mathbf{F} amongst models (\mathbf{F}_ρ). The Spearman
295 correlation coefficient for the factor profiles was chosen due to the expected non-linearity of the comparison and
296 likely presence of outliers. These comparisons, and especially when the ground truth is not available, need to be
297 accompanied by visual inspection of the solution quality, looking for resemblance with known environmental
298 sources. The models accounting for sparsity will be also compared upon the aforementioned Gini metric and,
299 when truth is available, the Gini ratio with truth and the “zero-truth sum”. Computational performance assessment
300 will be based on the metrics of convergence metrics of the Hamiltonian-Montecarlo Markov chain methods
301 embedded in STAN software (e.g. \hat{R}).

302

303 2.4 Datasets

304 The datasets created for model experimentation can be divided into synthetic and real-world datasets. Synthetic
305 datasets are artificially created with the purpose of knowing the \mathbf{F} , \mathbf{G} , to test model accuracy retrieving these
306 matrices with respect to the *truth* and these have been widely used for source apportionment validation in the last
307 decades (Park et al. 2002, Brinkman et al. 2006; Belis et al. 2015; Via et al. 2022; Rusanen et al. 2024). In order
308 to challenge the models gradually, we created three synthetic datasets with increasing degrees of complexities
309 (toy, offline, online ACSM synthetic datasets). Additionally, a real-world chemically sparse dataset was also used
310 to test the results. Although the truth factorisation is unknown and the results cannot be directly verified, the
311 model’s factorisation can be assessed environmentally or based on indicators on the goodness of fit. The different
312 datasets have different levels of sparsity, as can be seen in Table 2, that the models with the horseshoe prior should
313 aim to replicate. The time resolution of modelled OA sources, used both in the chemically-sparse toy dataset and
314 the chemically less sparse datasets, is 1 hour. The time resolution of offline datasets, used in the chemically sparse
315 synthetic offline dataset and the chemically-sparse real-world offline dataset is 1 day.

316 2.4.1 Chemically-sparse toy dataset

317 A simplistic synthetic toy dataset was designed as a deliberately simplified test case to perform basic control and
318 performance tests, rather than to reproduce any realistic atmospheric scenario. It was devised by creating three
319 very simple and sparse profiles and using three time series (HOA, SOA_{bio}, BBOA) from modelled source time
320 series of the city of Zurich (Rusanen et al. 2024, time resolution of 1h) in order to test how sparsity priors act on
321 very uneven species contribution. Although it is based on ACSM-like time series and therefore reflects some of
322 the temporal properties of such measurements, the three included sources do not represent combinations that
323 would be expected in a real-world environment since this toy dataset is intended solely for methodological testing
324 purposes. In addition, the source profiles were intentionally designed to be highly simplified in order to facilitate
325 an immediate visual assessment of the model fitting. For these reasons, the extracted components were not
326 assigned environmental labels, but were instead referred to generically as Factor 1, Factor 2, and Factor 3.

327

328 Then, \mathbf{F} and \mathbf{G} were multiplied to generate \mathbf{Z} , and some gaussian error with standard deviation σ was added to
329 each component to generate a realistic \mathbf{X} matrix. The uncertainties matrix σ was designed as a sixth of the \mathbf{X} values
330 plus Gaussian noise. With this arrangement, the models can be applied conventionally to the \mathbf{X} , σ matrices and
331 the modelled \mathbf{F} and \mathbf{G} , can be compared to the original truth \mathbf{F} , \mathbf{G} , which will be referred hereinafter as \mathbf{F}_0 and \mathbf{G}_0 ,
332 displayed in Figure S2.

333 2.4.2 Chemically-sparse synthetic offline dataset

334 We created a synthetic offline filter dataset, mimicking the filter-based measurements input matrices, in order to
335 test the accuracy of the models in these kinds of datasets. This dataset mimics the concentrations on the coarse
336 fraction ($\text{PM}_{10} - \text{PM}_{2.5}$) as collected by a high-volume sampler on the Zurich-Kaserne site (Grange et al. 2021)
337 including the following chemical species: OC, Al, Na, Mg, Cl, K, Ca, S, Fe, Cu, Zn, Mn, Sb, Ba, mannitol,
338 arabitol. In the original real-world dataset, data obtained with two series of samples (PM_{10} and $\text{PM}_{2.5}$) were
339 subtracted in order to focus on the coarse source apportionment, since the main emission sources of these elements
340 and organic species stem from mechanical processes leading to major coarse models. It was created by crafting
341 first the \mathbf{F} and \mathbf{G} , then multiply them and creating \mathbf{X} and σ . The \mathbf{F} matrix was slightly modified from that proposed
342 in Manousakas et al. (2025), making the chemical profiles slightly sparse by zeroing the non-relevant species in
343 each of the factors (dust, traffic, salt, coarse biological). The \mathbf{G} matrix was composed of the time series of:

- 344 - Dust: modelled PM_{10} dust (Vasilakos et al. in prep.) converted to coarse with the $\text{Al}_{\text{PM}_{10}}$ vs. PM_{10} ratio
345 from Grange et al. (2021).
- 346 - Traffic: modelled PM_{10} copper (Upadhyay et al. 2025) converted to coarse with the $\text{Cu}_{\text{PM}_{10}}$ vs. PM_{10}
347 ratio from Grange et al. (2021).
- 348 - Salt: coarse Na+Cl (Grange et al. 2021) converted to PM concentrations and multiplied by an arbitrary
349 number (3 in this case match the concentrations of the sea salt factor in the original dataset).
- 350 - Coarse biological: coarse Arabitol+Mannitol (Grange et al. 2021) converted to PM concentrations and
351 multiplied by 3, similarly as for the salt factor.

352 This dataset will be called “offline synthetic dataset”. Another more simplistic dataset was prepared similarly but
353 using Al and Cu for dust and traffic factors, respectively, in the same way as in the salt or coarse biological factors,
354 i.e. omitting the use of modelled data. This dataset will be hereinafter named “Purely-measurement-based offline
355 synthetic dataset” and its modelling results will be described in section 3.2. Once the \mathbf{F} and \mathbf{G} matrices were
356 created, \mathbf{X} was calculated by their multiplication and the addition of Gaussian noise with amplitude σ . The
357 uncertainties matrix σ was generated as in Grange et al. (2021) multiplied by 2 to balance the signal-to-noise ratio
358 to the datasets in Manousakas et al. (2025). The matrices \mathbf{F} , \mathbf{G} of this dataset are displayed in Figure S3.

359

360 2.4.3 Chemically sparse real-world offline dataset

361 A real-world dataset was employed to test the current models applicability in campaign measurements. This
362 dataset was originally used for source apportionment in Manousakas et al. (2025) and Grange et al. (2021) and
363 consists of $\text{PM}_{10-2.5}$ samples at five Swiss National Air Pollution Monitoring Network (NABEL): Basel, Bern,
364 Magadino, Payerne, and Zurich. The measurements were taken in the June 2018 - July 2019 period every fourth
365 day and using Digital high-volume samplers. During the sampling campaign PM_{10} and $\text{PM}_{2.5}$ were collected and

366 the respective concentrations were subtracted to generate the coarse ($PM_{10-2.5}$) concentrations. These samples
367 include: i. OC concentrations, measured through the thermal optical transmission (TOT) EN16909 method with
368 the EUSAAR2 temperature protocol; ii. elemental concentrations (Al, Fe, Cu, Zn, Mn, Sb, Ba, Sr, Bi, Pb)
369 measured by inductively coupled plasma atomic emission spectrometry (ICP-AES) and inductively coupled
370 plasma mass spectrometry (ICP-MS); iii. water soluble inorganic ion concentrations (Ca^+ , Cl^+ , Mg^+ , K^+ , Na^+),
371 determined by ion chromatography (IC); iv. Organic species (mannitol, arabitol) determined by a high-
372 performance liquid chromatographic method followed by pulsed amperometric detection (HPLC-PAD). The
373 uncertainties of these species were calculated as in Grange et al. (2021).

374 2.4.4 Chemically less sparse synthetic online ACSM datasets

375 With the aim of recreating more complex real-world datasets to test the models, we generated 6 datasets for four
376 European cities: Krakow, Milan, Paris, and Zurich. The objective was to recreate OA matrices as given by a mass
377 spectrometer instrument like Q-ACSM, for which there are plenty of real-world source apportionment studies in
378 the literature. The \mathbf{G} matrix was created from OA sources time series generated through the regional air quality
379 model CAMx (Comprehensive Air Quality Model with Extensions) as previously published by Jiang et al. (2019).
380 The five sources of these datasets were hydrocarbon-like OA (HOA), related to traffic emissions, biomass burning
381 OA (BBOA), biogenic SOA (SOA_{bio}), biomass burning SOA (SOA_{bb}), and traffic SOA (SOA_{tr}). To ensure
382 seasonal representativity while keeping computational costs low, datasets included the first two weeks of every
383 second month of 2011 (January, March, ...). The relative concentrations of these datasets are shown in Figure S5.
384 This figure shows the highest seasonal OA variation for the city of Milan and the lowest for Zurich. In terms of
385 sources, the most seasonally stable sources, overall, are HOA and SOA_{tr} in contrast to the remarkable variability
386 of BBOA and SOA_{bio} . The profiles used to create the species matrix \mathbf{F} were those in Table S2 for primary sources
387 (HOA, BBOA). For secondary sources, the profiles from the European megacity dataset presented in Rusanen et
388 al. (2024) were used for the Zurich city, which were slightly perturbed for the other cities due to the limited
389 availability of these sources' profiles in the literature.

390
391 The \mathbf{X} matrix was obtained by multiplying the \mathbf{F} and \mathbf{G} submatrices and adding Gaussian noise. The procedure to
392 calculate the error matrix for such datasets is described in Via et al. (2022) and the dataset used to calculate the
393 error matrix is that from the Zurich site, which ranges from February 2011 until December 2011.

394
395 Lastly, a sensitivity analysis was carried out by slightly modifying the original \mathbf{F} , \mathbf{G} matrices upon which the \mathbf{X} ,
396 σ matrices were subsequently created. The first Zurich dataset (period 01/09/2011 - 14/09/2011) was used for this
397 purpose and we chose to perturbate one factor only (HOA). The \mathbf{F} , \mathbf{G} submatrices were perturbed independently
398 upon the expression:

$$399 \quad G_{HOA}' = G_{HOA} \cdot N(1, \sigma') \quad F_{HOA}' = F_{HOA} \cdot N(1, \sigma') \quad (14)$$

400 where we used $\sigma' = [0, 0.1, 0.2, 0.3, 0.4, 0.5]$ to create different degrees of perturbation. The profiles in \mathbf{F} were
401 normalised after that process. It must be noted that the perturbation is more relevant on \mathbf{F} than in \mathbf{G} since a given
402 σ' in the aforementioned range is more comparable and impactful on the profile contributions, bounded to 1, than
403 on the unbounded time series timepoints. Consequently, within this framework, we obtained 6 \mathbf{G} -perturbed and 6
404 \mathbf{F} -perturbed input matrices. Both BAMF and BAMF+HS models were run with all these input matrices and their

405 subsequent HOA results were compared to the original truth in order to comprehend the sensitivity of the models
406 upon time series and profile perturbations.

407 **3. Results**

408 **3.1 Chemically sparse synthetic toy dataset**

409 Here, we introduce the evaluated models relying on unrealistically simplified toy data with the purpose of
410 showcasing the performance of the horseshoe prior introduction to BAMF (Figure S2) and the alternative
411 factorisation methodologies, which are discussed in SI Section C.1.

412
413 In the first evaluation step, we assess the performance of the horseshoe prior under the assumption that the source
414 matrix \mathbf{G} is known, in order to isolate its effect on the estimation of \mathbf{F} . Figure 1 shows the distribution of each \mathbf{F}
415 component for CMB with and without the horseshoe prior (CMB, CMB+HS, respectively, Table 1). The
416 distributions shown account for all the variability across samples of each \mathbf{F} component for both models, and the
417 truth is shown as a marker in the x-axis since it is a point value to be compared to the centers of the distributions.
418 The presentation of the CMB and CMB+HS distributions aims to demonstrate the sparsity-inducing role of the
419 horseshoe prior, which enforces shrinkage of the \mathbf{F} component toward zero; this effect is more readily discernible
420 when a strongly guided \mathbf{G} matrix is used to isolate the evidence of sparsity. Figure 1 showcases the horseshoe
421 prior power to generate sparsity in \mathbf{F} components, shrinking more strongly the lowest signals to zero than CMB
422 and, as a consequence, enlarging the most prominent signals. Table 3 shows how the Gini metric is consistently
423 higher for CMB+HS with respect to CMB, supported by a higher Gini ratio and lower zero truth metric reflecting
424 the sparsification of profiles and higher similarity to truth. The RMSE compared to the truth for the profiles
425 improved with the horseshoe prior applied for all three factors (for CMB and CMB+HS, respectively: $1.2\text{e-}04$,
426 $3.8\text{e-}05$ for F1; $1.86\text{e-}04$, $5\text{e-}05$ for F2; $3.3\text{e-}05$, $1\text{e-}05$ for F3). Hence, the sparsity introduced in \mathbf{F} through the
427 regularised horseshoe prior successfully improved the profile description of the solution.

428
429 In the next evaluation step, we test the various models assuming no prior knowledge. Figure 2 shows the results
430 of PMF, BAMF, and BAMF+HS models on the toy dataset and Table 3 shows their factorisation performance
431 and comparison to truth metrics. In terms of factorisation, median relative errors are better for BAMF+HS and
432 BAMF than for PMF, but their maximum errors are higher and the Pearson coefficients slightly lower, all this
433 entailing comparable factorisation performances. All models generally adapt well to the truth features, but they
434 present non-negligible differences. PMF results better resemble the truth in terms of $\mathbf{G} R^2$, but it is the model
435 whose G/G_0 differs from 1 the most, accumulating the greatest error (2.64), followed by BAMF (2.10), while
436 BAMF+HS exhibits the smallest deviation (0.81), indicating the highest overall accuracy. In terms of profiles, the
437 BAMF+HS model is the closest to the truth both in terms of ρ and R^2 , especially for the second and third factors
438 for which the sparsity introduction results are advantageous with respect to BAMF results. Consistently, the Gini
439 ratios of the inferred solutions relative to the truth are markedly closer to unity for BAMF+HS (range 0.40–0.93)
440 than for PMF (0.45–0.64). The sparsity effects can also be seen in Figure S5, in which the horseshoe shrinkage is
441 evident for the low m/z s allowing in turn the larger m/z s to retain more mass, hence resembling better the truth
442 profiles. Taken together, these results indicate that BAMF+HS not only promotes sparsity, but does so in a

443 chemically consistent manner, leading to a more accurate mass apportionment across factors, despite a slightly
444 reduced time-series correlation for the third factor. However, the BAMF+HS could not shrink down the lowest
445 signals in Factor 1, likely because their contribution estimated by the mass balance and the autocorrelation
446 restrictions of this model made it unclear for the horseshoe to shrink them down completely. With this result, this
447 toy dataset depicts the capacities and limitations of the horseshoe implementation on BAMF: it is capable to
448 sparsify effectively only the signals which are close enough to zero as given by the restrictions of the BAMF
449 model.

450 While other sparsity priors exist (e.g. Lasso and Spike-and-slab priors (Figure S6, Table 3, Table S3)), our tests
451 show that the BAMF+HS model is most effective in shrinking unnecessary contributors to F . Hence this prior
452 will be used onwards. This is evidently portrayed by the Gini ratio, for which neither Lasso nor Spike-Slab achieve
453 the signal shrinkage that the BAMF+HS does. Also, neither BAMF+Lasso nor BAMF+Spike-and-slab managed
454 to sparsify the first factor. Additionally, different autocorrelation formulations were implemented with and
455 without the horseshoe prior, showing worse performance than BAMF or BAMF+HS, respectively, as discussed
456 in section SI C.1. This supports using the BAMF autocorrelation prior instead of the alternative AR(1) prior, G
457 simplex formulation or lack of autocorrelation prior models, although these models are also tried on the other
458 datasets to further highlight this.

459 3.2 Chemically sparse synthetic offline dataset

460 This synthetic offline dataset was used to assess the performance of different models on a proxy representation of
461 atmospheric aerosol data, while maintaining the verifiability property inherent to synthetic datasets as described
462 in Section 2.4.2. We performed source apportionment of the X matrix through the aforementioned Bayesian
463 models and PMF, obtaining 4 factors fingerprints and time series. The dataset used in this source apportionment
464 is expected to be much more sparse than ACSM-like datasets, hence it could better expose the capabilities and
465 added value of the sparsity prior.

466
467 To avoid initialisation failure, BAMF was run by initialising F as a normal distribution to ensure a more sturdy
468 sampling. Model initialisation fails when no set of initial parameter values satisfying the model result in valid
469 Bayesian solutions, and are usually solved by imposing more informative priors constraints on the model
470 parameters. A t-test was run comparing the F , G factors from this slightly modified model and BAMF to ensure
471 their similarity. Its results passed the t-test for all factors except for one factor, although it presented a $R^2=0.9990$
472 correlation and only a 20% of quantitative difference with that BAMF factor. Hence, one can assume that the
473 model provides an acceptable level of agreement with BAMF, capturing the essential structure of the factors with
474 only very minor deviations.

475
476 Figure 3 presents the (a) time series (b) auto-correlation (c) profiles of the source apportionment solution for PMF,
477 BAMF, BAMF+HS, (d) additional comparison to truth metrics, and Figure 4 shows the histograms of the models
478 F components estimation. The time series and autocorrelation show only slight differences between the models,
479 the PMF being the most different to the truth in all factors except the salt one, as supported in Figure 3 (d).
480 Amongst factors, the coarse biological source is the most poorly reconstructed. If accounting for the sum of all
481 factors G R^2 's and G/G_0 , in the last row of Figure 3(d), the most accurate model is the BAMF+HS, followed by

482 PMF and then BAMF. In terms of profiles, the best overall model performance depends on the metric, **F** Spearman
483 correlation coefficient being highest for BAMF and R^2 and cosine similarity correlation coefficients for
484 BAMF+HS. This fact, accompanied by Gini being the highest for BAMF+HS and the closest to 1 Gini ratio,
485 indicates that the extreme values of the profile (i.e. maximum and zeros species contributions) are closer to truth
486 for BAMF+HS, whose extreme contributions would be less relevant in the Spearman correlation coefficient.
487 Considering the Truth **F** zeros sum metric, the horseshoe shrinkage is visibly sparsifying most of the low signals
488 whilst BAMF and PMF present non-zero contributions for species whose contribution in this factor is null. Hence,
489 the BAMF+HS model would effectively promote the profiles sparsity which it was intended for.

490
491 However, the favourable results of BAMF+HS in comparison to the other models could be a dataset-dependent
492 finding, related to the properties of the created synthetic dataset. The purely-measurement-based offline synthetic
493 dataset, whose performance statistics are shown in Table S4, shows that PMF overperforms BAMF+HS,
494 presenting slightly higher **F** and **G** R^2 and better G/G_0 . This could indicate that the optimal model selection might
495 be dataset dependent. However, the source time series of this very simplistic dataset are fully correlated with some
496 species time series, since they are used to generate factor time series, which makes it a very redundant dataset. In
497 this scenario, the source apportionment comparison might still be valid, but it is not the perfect showcase for RMs
498 testing due to the excessive source correlation with species. We found it valuable to present different model
499 performances on different datasets, which in atmospheric measurements, can suffer from artefacts complicating
500 the behaviour of some models.

501
502 In the same way, the alternative autocorrelation priors models were also tried and will be thoroughly discussed in
503 Section SI C.II. However, overall, the BAMF+HS model is the one providing the best source apportionment
504 results for this offline dataset, taking advantage of the sparsity to upgrade both profiles and time series accuracy.
505

506 3.3 Real-world offline dataset

507 To test the models on real-world data and identify their limitations for more complex datasets, we tested the
508 models in the real-world offline PM_{10} - $PM_{2.5}$ dataset described in Section 2.4.3. Since the truth is not accessible,
509 the model performance can only be assessed upon environmental, factorisation-related, and computational criteria.
510 For this dataset, BAMF and BAMF-AR1 models presented initialisation issues preventing them from properly
511 launching the models. To avoid this issue and make the model more robust, we implemented a prior in **F** so that
512 its components are drawn from Gaussian distributions centered at zero and with a standard deviation of 1 so that
513 we restrict values to be bounded to 1. This modification was not needed for the other models, which did not present
514 initialisation issues.

515
516 Source apportionment results for PMF, BAMF, and BAMF+HS are shown in Figure 5 and Table 4. Figure 6
517 shows the **F** distributions for these models, as a detail of Figure S9 (a). Figure S6, S9 (a) display very similar
518 results for PMF, BAMF, BAMF+HS both in terms of **F**, **G**, and reconstruction metrics, and only some differences
519 can be perceived for PMF, while BAMF and BAMF+HS histograms are almost overlapping in Figure 6. However,
520 the BAMF+HS profiles present a remarkable difference in terms of sparsity as seen in the **F** Gini metric, which is

521 mostly the highest for BAMF+HS or equal, except for the biological factor for which PMF is slightly higher. For
522 some species, the relative \mathbf{F} components apportionment is more strongly suppressed by BAMF+HS than by
523 BAMF or PMF, hence, their contribution on other profiles can be larger. This is clearly visible, for instance, for
524 OC, Mg^+ , K^+ , S^+ , or mannitol, which are zeroed in the Salt factor and consequently are larger on the factors where
525 these species are relevant. This is more evidently depicted in Figure S9 (a) and Figure 6, where the distribution of
526 \mathbf{F} components is shown. For the aforementioned species, the horseshoe effect can be seen in the distribution,
527 whilst BAMF and PMF are further from zero. This result thus highlights the potential benefits of sparsity
528 introduction in matrix factorisation.

529
530 The application of other autocorrelation priors was not advantageous with respect to the regular BAMF
531 autocorrelation and even worsened the shrinkage power of the horseshoe prior as discussed in SI C.III.

532 3.4 Chemically less sparse synthetic online ACSM datasets

533 The next step was to test these models on more realistic synthetic datasets. For that purpose, 6 datasets for 4
534 European cities (a total of 24 datasets) were designed with 5 factors in each of them (section 2.4). We applied the
535 8 models under discussion (PMF, BMF, BMF+HS, BAMF, BAMF+HS, BAMF-AR1, BAMF-GS) to the 24
536 synthetic datasets and computed the summary statistics (the median of the ratios of \mathbf{G} over the truth \mathbf{G} , \mathbf{G}/\mathbf{G}_0 , the
537 Pearson correlation of \mathbf{G} with truth, $\mathbf{G} r$, and the Spearman correlation of \mathbf{F} with truth, $\mathbf{F} \rho$). All metrics over cities,
538 datasets and sources are presented in Table S5, and an example for one site (Zurich) and one dataset (dataset 0,
539 from 01/01/2019 to 14/01/2019) is shown in Figure S11 as an example of the results obtained by the three models
540 in 1 out of the 24 datasets.

541
542 Figure 7 shows the model summary statistics over the 6 generated datasets for the four cities and Figure S12 shows
543 the factor-dependent statistics. In this case, the (not-squared) Pearson correlation coefficient was used to compare
544 the results of the ACSM-like datasets more easily to those presented in Rusanen et al. (2024), which used this
545 metric. Figure 7 shows a good agreement between models and the truth, with most solutions with correlations
546 with truth for \mathbf{F} and \mathbf{G} above 0.7, similarly to Rusanen et al. (2024). However, there are clear differences amongst
547 models and cities. PMF is performing worse in comparison to the Bayesian models, including BMF, the Bayesian
548 analog to PMF in all datasets except for Milan. As shown in Table S5, PMF presents the highest $|\mathbf{Z}-\mathbf{X}|/\sigma$, the
549 highest overestimations of \mathbf{G} , and correlations of \mathbf{G} and \mathbf{F} are the lowest in comparison to other models except for
550 the Milan dataset. In terms of \mathbf{G}/\mathbf{G}_0 , the model providing the best results are BAMF, BAMF-AR1, BAMF-GS,
551 followed by their horseshoe versions. The BAMF+HS, presents slightly lower $\mathbf{F} \rho$, $\mathbf{F} R^2$, and the sparsity Gini
552 metric ratio is not close to one, entailing the horseshoe prior did not successfully implement sparsity and the \mathbf{F}
553 accuracy did not improve. In terms of correlations with \mathbf{F} and \mathbf{G} , the models including the horseshoe prior present
554 higher dispersion within a city with respect to the models without sparsity terms. Considering all the parameters,
555 the models with the best overall performance are BAMF, BAMF-GS, and BAMF+HS.

556
557 Figure S13 shows the autocorrelation for lags 0-168 h (half of the monthly measurement period) for all the sources
558 and sites, displaying the cyclicity of the selected sources. In all cases, the short-term lags present very high
559 autocorrelation, entailing that the similarity on adjacent timestamps is very high and decays over longer periods.

560 Typically, and as presented on the figure, the autocorrelation of primary sources, with more marked daily cycles,
561 decays faster than secondary sources, which evolve more steadily due to their slower reaction to emissions. Whilst
562 HOA and BBOA present a very steady intradaily structure, with one or two maxima per day, the biogenic SOA
563 presents one peak per day and the other two secondary sources may or may not present marked daily cycles. This
564 different intra- and inter-daily structure amongst sources certainly challenges the models to resolve the source-
565 dependent characteristic.

566
567 Figure 8 shows the autocorrelation from truth and the model outputs correlate (Pearson coefficient of
568 determination) for each model and source in the 4 cities. Each dot represents one of the 6 datasets for each site,
569 and colors represent the different sources. The results show that all models present very high Pearson coefficient
570 ranges for **G** autocorrelations in comparison to truth except for PMF, which struggles with this dataset aspect due
571 to the lack of accounting of self-correlation. In general terms, the best captured correlation by all models is that
572 of SOA_{Bio}, with the most regular cyclical patterns. The SOA_{BB} and SOA_{Tr} autocorrelations seem to challenge the
573 models further due to more irregular patterns, and for some datasets, their autocorrelation is poorly modeled. POA
574 sources are generally accurately modelled, with HOA patterns slightly better captured than those from BBOA.
575 Regarding models, the ones with better performance are BAMF-GS, BAMF, and BAMF+HS, with only slight
576 differences between the last two. This observation suggests that the horseshoe prior addition does not significantly
577 reduce the autocorrelation power of the BAMF.

578
579 Regarding sparsity, Figure S14 depicts the lack of sparsity both for input and modelled data. This figure shows
580 the truth's 5 lowest m/z components as well as BAMF, BAMF+HS outcomes. The reference (truth) profiles do
581 not present zeros but very small signals, as do many ACSM-like profiles in the AMS spectral database (Ulbrich
582 et al. 2009). Both BAMF, BAMF+HS reflect this lack of sparsity, however, it could be expected that BAMF+HS
583 would decrease the contributions of the lowest components. However, the sparsity introduction was not achieved
584 as seen before in the lack of improvement of the Gini ratios. This lack of sparsity despite the enforcement through
585 the horseshoe prior can be explained by the complexity of the data, which due to chain divergence, hinders the
586 models performance. Figure S15 shows the model \hat{R} , a typical Bayesian metric to evaluate the precision of
587 Hamiltonian chains, computing the ratio between inter- and intra-chain variabilities. In any case results are very
588 close to the ideal value, 1, so the validity of all models' solutions is assured. However, this plot reflects the
589 deprecation of the solution with models when the horseshoe prior is applied. The horseshoe prior adds more
590 complexity to the **F** with three more parameters compared to non-sparsity models which could be the cause of the
591 increased model instability across chains.

592
593 Finally, a sensitivity analysis was run for the first Zurich dataset perturbing independently the original **F**, **G**
594 matrices to different degrees, monitoring the correlation of the modelled **F**, **G** matrices to the original truth (Figure
595 9). Subfigures (a) and (b) show how both in the case of the original **F** and **G** perturbations, the **F** accuracy drops
596 immediately and analogously for both models, with a more sudden decay for **G** perturbations. Contrarily, the
597 affectations in **G** (subplots (c) and (d)) are different for both models, with a steady decay for BAMF with **G**
598 perturbations and a non-clear trend for **F** perturbations, whilst BAMF+HS correlation rests insensitive to **F**, **G**
599 perturbations with an increasing/decreasing erratic behaviour. This result shows the reduced precision in **G** of

600 BAMF+HS in comparison to BAMF due to the chain divergence issue, which, in any case, does not severely
601 compromise its accuracy. This finding also explains the bigger variations for BAMF+HS with respect to BAMF
602 in all the metrics shown in Figure 8. Additionally, it showcases the general strong sensitivity of \mathbf{F} determination
603 opposite to the general robustness of \mathbf{G} upon general \mathbf{X} matrix perturbation.

604 ~~3.~~ 4. Discussion

605 This study aims to explore further BAMF capabilities and the benefits introduced through additional priors and/or
606 modifications of the current model structure as given by Rusanen et al. (2024). The introduction of sparsity in
607 source apportionment models was of particular interest to provide more distinct and concise source profiles which
608 can, in turn, improve the time series accuracy. However, in real-world applications, it may also remove small but
609 relevant signals along with noise. Therefore, comparison with BAMF results is recommended, leaving it to the
610 user to decide whether the method's use is appropriate for their case.

611
612 Firstly, the use of the simplistic toy dataset highlighted the added value of the sparsity introduction through the
613 horseshoe prior in the totally constrained experiment. In this controlled setting, the ground truth structure is well
614 defined, allowing the effect of sparsity to be clearly isolated and the method performance validated. However, for
615 an unconstrained experiment, sparsity was proven remarkably advantageous, but subject to the underlying matrix
616 factorisation results. That is, the horseshoe prior in BAMF+HS effectively suppresses weak signals of \mathbf{F}
617 contributions as determined by BAMF, yet it fails to guide the model toward a more accurate or sparser solution
618 when the initial BAMF estimate is suboptimal. Other sparsity priors, like Lasso and Spike-and-slab, were tried
619 out but did not improve the regularised horseshoe performance.

620
621 The introduction of the regularised horseshoe prior in BAMF improved apportionment of offline synthetic and
622 real-world datasets with respect to BAMF, promoting sparser profiles. The synthetic dataset comparison to truth
623 was maximal for BAMF+HS, with sparser profiles and consequently better \mathbf{G} accuracy. Its application also proved
624 advantageous for the real-world dataset, despite not being able to be compared to the truth. In this case,
625 improvements are assessed through increased profile distinctness and internal consistency rather than absolute
626 accuracy. The results show a sparsity effect which provides more distinct profiles in comparison to PMF and
627 BAMF. This result encourages the usage of the horseshoe prior for sparsity introduction in datasets whose
628 solutions are expected to be strongly sparse, such as elemental datasets.

629
630 Subsequently, in the more complex and realistic European datasets, the sparsity introduction could not be
631 effectively enforced. Although solution quality was not substantially compromised, the profiles remained non-
632 sparse after applying the prior. This is likely due to model instability arising from the higher complexity of these
633 datasets, which is further aggravated by the addition of the horseshoe prior, as it requires sampling a larger number
634 of parameters. Moreover, the inherent nature of ACSM datasets—characterized by highly correlated species—
635 might also contribute to this limitation, since the model struggles to disentangle overlapping sources when
636 variables are strongly interdependent. The higher chain divergence found for the *horseshoed* models causes a drop
637 in solution precision due to different landings on the solution space depending on the chain. This issue could be
638 reduced by selecting chains a-posteriori upon user-defined criterion as is practiced in PMF. This is further

Formatted: Indent: Left: 0.63 cm, Hanging: 0.63 cm,
No bullets or numbering

Formatted: English (United States)

639 confirmed by the insensitivity to \mathbf{G} or \mathbf{F} perturbations that are visible for BAMF+HS but not for BAMF.
640 Nonetheless, given that ACSM-like factor profiles exhibit low sparsity in the literature, the use of sparsity priors
641 in these datasets is less justified. Also, because usually ACSM profiles obtained in chamber or ambient
642 experiments are not usually sparse, as seen in Ulbrich et al. (2009), the BAMF+HS is not as pertinent in these
643 kinds of datasets as for filter-based datasets.

644
645 The sparsity conceptual framework could also be brought into PMF through the pulling equations, which can
646 shrink down manually the expectedly low signals in a factor. However, this methodology requires that the user
647 indicates the species that are intended to be zeroed, which introduces user-subjectivity to the problem. The
648 BAMF+HS method, contrarily, acts globally, shrinking those species with lowest signals in favour of the matrix
649 factorisation, hence no user intervention is needed. This makes the approach more objective but also less targeted,
650 returning the factorization optimisation agency to the model. However, if the purpose were to enforce a shrinkage
651 of a certain species as in the PMF case, this feature could also be implemented through the horseshoe method with
652 minimal code modification.

653
654 The results of the other models tested (BAMF-AR1, BAMF-GS) did not show a significant improvement with
655 respect to BAMF. The BAMF-AR1 contains another autocorrelation to parametrisation (STAN Team, 2025)
656 which should allow for trend consideration, although this matter was not tackled in the current work and remains
657 to be validated in future studies. The BAMF-GS seemed to capture slightly better the \mathbf{G} variability in comparison
658 to BAMF in the online datasets, but led to worse correlation to truth in the offline synthetic dataset. Nonetheless,
659 it does not support enforcing sparsity in \mathbf{F} , thereby reducing its effectiveness for profile adjustments.

660 ~~4.~~ 5. Conclusions

661 This study presents a sparsity introduction technique for the Bayesian Autocorrelated Matrix Factorisation model
662 (BAMF) which intends to condense source apportionment profiles removing noisy signals. The regularised
663 horseshoe prior, [a tool to promote sparsity in datasets](#), is introduced in BAMF (BAMF+HS) in order to narrow
664 down the lowest signals in factor profiles while keeping the most significant ones regularised. The BAMF+HS
665 model is built in STAN, an open-source framework for statistical modelling with Hamiltonian-Montecarlo
666 Markov Chain sampling. In order to test the capabilities of the developed model, we generated three kinds of
667 synthetic datasets to compare the model factorisation outputs to the truth factors, namely Toy, offline, and online
668 synthetic datasets, each representing a progressively increasing level of complexity. Likewise, to confirm its
669 usability to real-world data, BAMF+HS was also applied to a multi-site filter dataset. Given the opportunity to
670 explore source apportionment with different types of datasets, we also tested other receptor models such as
671 Positive Matrix Factorisation (PMF) and other BAMF-like Bayesian models. In the Bayesian framework, we
672 tested a different formulation of the autocorrelation term (BAMF-AR1) and a permutation on the factorisation
673 matrix logic (BAMF-GS).

674 The main result highlights can be summarised as:

- 675 - BAMF+HS has been shown to be advantageous to introduce sparsity in factor profiles for offline datasets
676 and to not deprecate the solution for the more complex datasets mimicking Aerosol Chemical Speciation
677 Monitor (ACSM) data. Other sparsifying priors tried out were not as effective in low-signal shrinkage.

Formatted: No bullets or numbering

Formatted: English (United States)

- 678 - The BAMF+HS performance towards truth profile reconstruction was higher than for BAMF and PMF
679 in the toy and offline synthetic datasets. Improving \mathbf{F} typically led to a more accurate determination of
680 \mathbf{G} , highlighting the strong interdependence between the two factorisation matrices.
- 681 - The real-world dataset also shows a better description of sources through BAMF+HS in terms of matrix
682 factorisation metrics and profile sparsification achievement.
- 683 - As shown in the toy dataset, the introduction of sparsity did not solve factorisation issues inherent to the
684 underlying factorisation model.
- 685 - The BAMF+HS model does not create sparsity in ACSM-like datasets, which are originally, indeed, non-
686 sparse. BAMF+HS is more unstable than BAMF for these more complex datasets as a result the higher
687 chain divergence during Hamiltonian-Montecarlo Markov Chain sampling as suggested by the \hat{R} metric.
688 However, the effects of the horseshoe prior do not affect the overall performance of BAMF or its
689 autocorrelation accuracy.
- 690 - The alternative formulations for BAMF, BAMF-AR1 and BAMF-GS, did not show a significant
691 improvement with respect to BAMF.

692 With all that, profile sparsity has been shown to substantially enhance the accuracy of source apportionment
693 analyses, improving the separation of the chemical composition of sources. The BAMF+HS model succeeds in
694 incorporating this property in profile fingerprints, especially in filter-based datasets. Using BAMF+HS in such
695 datasets, the solutions reflect the sparsity of filter-based chemical profiles, hence, this newly introduced method
696 is encouraged when source fingerprints are expected to be substantially sparse. However, for ACSM-like datasets,
697 the sparsity is not fully achieved due to converge issues, although the quality of the solution is not substantially
698 deprecated with respect to BAMF. With the aim of improving further source apportionment techniques, future
699 research should be directed to enhance the robustness and generalisability of the BAMF+HS model across diverse
700 data types. Moreover, continued exploration of the underlying properties of solution spaces (such as **profiles**
701 **profile** sparsity, time series autocorrelation) may provide valuable insights into disentangling complex source
702 contributions through receptor modelling. In this regard, the Bayesian source apportionment framework offers a
703 particularly suitable foundation, allowing for the integration of prior knowledge and uncertainty quantification in
704 the inference process.

705 **Code and data availability**

706 The models and datasets can be found at <https://github.com/martavia0/BAMF-horseshoe.git>

707 **Author contribution**

708 MV: Conceptualisation, data curation, formal analysis, funding acquisition, investigation, methodology, project
709 administration, resources, software, validation, visualisation, writing (original draft preparation). YH: Formal
710 analysis, investigation, software; JD: investigation, resources, software, validation. MM: Data curation. AR: Data
711 curation, formal analysis, methodology, investigation, resources, software. JJ: Data curation. SKG: Data curation.
712 J-LJ: Data curation; VNTD: Data curation. GU: Data curation. GM: conceptualisation, funding acquisition,
713 investigation, supervision, validation. KRD: Conceptualisation, data curation, formal analysis, funding

714 acquisition, investigation, methodology, supervision, validation. All co-authors participated in the revision and
715 edition of the manuscript.

716

717 **Competing interests**

718 The authors declare that they have no conflict of interest.

719

720 **Disclaimer**

721

722 Co - funded by the European Union. Views and opinions expressed are however those of the author(s) only and
723 do not necessarily reflect those of the European Union or European Research Exacutive Agency. Neither the
724 European Union nor the granting authority can be held responsible for them.

725 **Acknowledgements**

726 This publication is co- funded by/ has received funding from/ the European Union 's Horizon Europe research and
727 innovation program under the Marie Skłodowska-Curie COFUND Postdoctoral Programme grant agreement
728 No.101081355- SMASH and by/from /the Republic of Slovenia and the European Union from the European
729 Regional Development Fund. Work was partly supported by ARIS program P1-0385. All the chemical
730 measurements on the PM10 and PM2.5 Swiss samples used in this study were performed on the Air O Sol
731 analytical plateau at IGE (France). K.R.D. acknowledges support by the SNSF Ambizione grant PZPGP2_201992.
732 The authors thank Jimeng Wu and Imad El Haddad for their input related to autocorrelation.

733

734 **References**

- 735 Andersen, M. R., Winther, O., & Hansen, L. K. (2014). Bayesian inference for structured spike and slab
736 priors. *Advances in Neural Information Processing Systems*, 27.
- 737 Belis, C. A., Karagulian, F., Larsen, B. R., & Hopke, P. K. (2013). Critical review and meta-analysis of ambient
738 particulate matter source apportionment using receptor models in Europe. *Atmospheric Environment*, 69, 94-108.
- 739 Belis, C. A., Larsen, B. R., Amato, F., El Haddad, I., Favez, O., Harrison, R. M., ... & Viana, M. (2014). European
740 guide on air pollution source apportionment with receptor models. JRC reference reports EUR26080 EN.
- 741 Belis, C., Pernigotti, D., Karagulian, F., Pirovano, G., Larsen, B., Gerboles, M., and Hopke, P.: A new
742 methodology to assess the performance and uncertainty of source apportionment models in intercomparison
743 exercises, *Atmospheric Environment*, 119, 35–44, 2015.
- 744 Brinkman, G., Vance, G., Hannigan, M. P., and Milford, J. B.: Use of synthetic data to evaluate positive matrix
745 factorization as a source apportionment tool for PM2. 5 exposure data, *Environmental science & technology*, 40,
746 1892–1901, 2006.
- 747 Carpenter, B., Gelman, A., Hoffman, M. D., Lee, D., Goodrich, B., Betancourt, M., ... & Riddell, A. (2017). Stan:
748 A probabilistic programming language. *Journal of statistical software*, 76, 1-32.

749 Crippa, M., DeCarlo, P. F., Slowik, J. G., Mohr, C., Heringa, M. F., Chirico, R., ... & Baltensperger, U. (2013).
750 Wintertime aerosol chemical composition and source apportionment of the organic fraction in the metropolitan
751 area of Paris. *Atmospheric Chemistry and Physics*, 13(2), 961-981.
752 Dai, T., Dai, Q., Yin, J., Chen, J., Liu, B., Bi, X., ... & Feng, Y. (2024). Spatial source apportionment of airborne
753 coarse particulate matter using PMF-Bayesian receptor model. *Science of The Total Environment*, 917, 170235.
754 Daellenbach, K. R., Uzu, G., Jiang, J., Cassagnes, L. E., Leni, Z., Vlachou, A., ... & Prévôt, A. S. (2020). Sources
755 of particulate-matter air pollution and its oxidative potential in Europe. *Nature*, 587(7834), 414-419.
756 Daellenbach, K. R., Manousakas, M., Jiang, J., Cui, T., Chen, Y., El Haddad, I., ... & Prévôt, A. S. H. (2023).
757 Organic aerosol sources in the Milan metropolitan area—Receptor modelling based on field observations and air
758 quality modelling. *Atmospheric Environment*, 307, 119799.
759 Dinh, V. N. T., Uzu, G., Dominutti, P., Sauvage, S., Elazzouzi, R., Darfeuil, S., Voiron, C., Samaké, A., Zhang,
760 S., Socquet, S., Favez, O., and Jaffrezo, J.-L.: Toolbox for accurate estimation and validation of PMF solutions in
761 PM source apportionment, *EGUsphere* [preprint], <https://doi.org/10.5194/egusphere-2025-1968>, 2025.
762 Elser, M., Huang, R. J., Wolf, R., Slowik, J. G., Wang, Q., Canonaco, F., ... & Prévôt, A. S. (2016). New insights
763 into PM 2.5 chemical composition and sources in two major cities in China during extreme haze events using
764 aerosol mass spectrometry. *Atmospheric Chemistry and Physics*, 16(5), 3207-3225.
765 Gelman, A., & Rubin, D. B. (1992). Inference from Iterative Simulation Using Multiple Sequences. *Statistical*
766 *Science*, 7(4), 457–472. <https://doi.org/10.1214/ss/1177011136>
767 Gelman, A., Carlin, J. B., Stern, H. S., Dunson, D. B., Vehtari, A., and Rubin, D. B.: *Bayesian data analysis*, 3rd
768 edn., CRC Press, ISBN 9781439898208, 2014.
769 Gini, Corrado (1936). "On the Measure of Concentration with Special Reference to Income and Statistics",
770 Colorado College Publication, General Series No. 208, 73–79
771 Govan, E., Jackson, A. L., Inger, R., Bearhop, S., & Parnell, A. C. (2023). *simmr*: A package for fitting stable
772 isotope mixing models in R. *arXiv preprint arXiv:2306.07817*.
773 Grange, S. K., Fischer, A., Zellweger, C., Alastuey, A., Querol, X., Jaffrezo, J. L., ... & Hueglin, C. (2021).
774 Switzerland's PM10 and PM2.5 environmental increments show the importance of non-exhaust emissions.
775 *Atmospheric environment: X*, 12, 100145.
776 Hoffman, M. D. and Gelman, A.: The No-U-Turn sampler: adaptively setting path lengths in Hamiltonian Monte
777 Carlo, *J. Mach. Learn. Res.*, 15, 1593–1623, 2014.
778 Jiang, J., Aksoyoglu, S., El-Haddad, I., Ciarelli, G., Denier van der Gon, H. A., Canonaco, F., ... & Prévôt, A. S.
779 (2019). Sources of organic aerosols in Europe: A modelling study using CAMx with modified volatility basis set
780 scheme. *Atmospheric Chemistry and Physics Discussions*, 2019, 1-35.
781 Keuken, M. P., Moerman, M., Voogt, M., Blom, M., Weijers, E. P., Röckmann, T., & Dusek, U. (2013). Source
782 contributions to PM2.5 and PM10 at an urban background and a street location. *Atmospheric Environment*, 71,
783 26-35.
784 Kuhn, H. W. (1955). The Hungarian method for the assignment problem. *Naval research logistics quarterly*, 2(1-
785 2), 83-97.
786 Lingwall, J. W., & Christensen, W. F. (2007). Pollution source apportionment using a priori information and
787 positive matrix factorization. *Chemometrics and Intelligent Laboratory Systems*, 87(2), 281-294.

788 Liu, D. C. and Nocedal, J.: On the Limited Memory BFGS Method for Large Scale Optimization, *Math. Program.*,
789 45, 503–528, <https://doi.org/10.1007/BF01589116>, 1989.

790 Manousakas, M. I., Rausch, J., Jaramillo Vogel, D., Schneider-Beltran, K., Alastuey, A., Jaffrezo, J. L., ... &
791 Dällenbach, K. R. Comparison of PM Source Profiles Identified by Different Techniques and the Potential of
792 Utilizing Single-Particle Analysis Data in Source Apportionment. Available at SSRN 5323830.

793 Metropolis, N., Rosenbluth, A. W., Rosenbluth, M. N., Teller, A. H., & Teller, E. (1953). Equation of state
794 calculations by fast computing machines. *The Journal of Chemical Physics*, 21(6), 1087–1092.
795 <https://doi.org/10.1063/1.1699114>

796 Oh, M. S., & Park, C. K. (2022). Regional source apportionment of PM_{2.5} in Seoul using Bayesian multivariate
797 receptor model. *Journal of Applied Statistics*, 49(3), 738-751.

798 Paatero, P., & Tapper, U. (1994). Positive matrix factorization: A non-negative factor model with optimal
799 utilization of error estimates of data values. *Environmetrics*, 5(2), 111-126.

800 Paatero, P. (1999). The multilinear engine—a table-driven, least squares program for solving multilinear
801 problems, including the n-way parallel factor analysis model. *Journal of Computational and Graphical Statistics*,
802 8(4), 854-888.

803 Park, E. S., Guttorp, P., & Henry, R. C. (2001). Multivariate receptor modeling for temporally correlated data by
804 using MCMC. *Journal of the American Statistical Association*, 96(456), 1171-1183.

805 Park, E. S., Spiegelman, C. H., & Henry, R. C. (2002). Bilinear estimation of pollution source profiles and amounts
806 by using multivariate receptor models. *Environmetrics*, 13(7), 775-798.

807 Park, E. S., Lee, E. K., & Oh, M. S. (2021). Bayesian multivariate receptor modeling software: BNFA and
808 bayesMRM. *Chemometrics and Intelligent Laboratory Systems*, 211, 104280.

809 Piironen, J. and Vehtari, A.: Sparsity information and regularization in the horseshoe and other shrinkage priors,
810 *Electronic Journal of Statistics*, 11, 5018–5051, <https://doi.org/10.1214/17-EJS1337SI>, 2017.

811 Rasmussen, M. A., & Bro, R. (2012). A tutorial on the Lasso approach to sparse modeling. *Chemometrics and
812 Intelligent Laboratory Systems*, 119, 21-31.

813 Pope III, C. A., & Dockery, D. W. (1999). Epidemiology of particle effects. In *Air pollution and health* (pp. 673-
814 705). Academic Press.

815 Rusanen, A., Bjorklund, A., Manousakas, M. I., Jiang, J., Kulmala, M. T., Puolamaki, K., and Daellenbach, K.
816 R.: A novel probabilistic source apportionment approach: Bayesian auto-correlated matrix factorization,
817 *Atmospheric Measurement Techniques*, 17, 1251–1277, <https://doi.org/10.5194/amt-17-1251-2024>, 2024.

818 Sage, A. M. (2007). Evolving mass spectra of the oxidized component of organic aerosol mass spectrometer
819 analysis of aged diesel emissions. *Atmos. Chem. Phys. Discuss.*, 7, 10065-10096.

820 STAN Development Team. (2025). *Stan user's guide* (Version 2.36), <https://mc-stan.org/docs/stan-users-guide/>.
821 Accessed July 2025.

822 Tobler, A. K., Skiba, A., Canonaco, F., Močnik, G., Rai, P., Chen, G., ... & Prevot, A. S. (2021). Characterization
823 of non-refractory (NR) PM₁ and source apportionment of organic aerosol in Kraków, Poland. *Atmospheric
824 chemistry and physics*, 21(19), 14893-14906.

825 Tibshirani, R., & Wasserman, L. (2015). Sparsity and the lasso. *Statistical machine learning*, 1-15.

826 Ulbrich, I. M., Handschy, A., Lechner, M., and Jimenez, J. L.: AMS Spectral Database,
827 <http://cires.colorado.edu/jimenez-group/AMSsd/>, accessed: 2025-05-19, n.d.

Field Code Changed

Field Code Changed

Field Code Changed

828 Ulbrich, I. M., Canagaratna, M. R., Zhang, Q., Worsnop, D. R., & Jimenez, J. L. (2009). Interpretation of organic
829 components from Positive Matrix Factorization of aerosol mass spectrometric data. *Atmospheric Chemistry and*
830 *Physics*, 9(9), 2891-2918.

831 Upadhyay, A., Jiang, J., Cheng, Y., Vasilakos, P., Chen, Y., Banos, D. T., ... & El-Haddad, I. (2025). High-
832 resolution modelling of particulate matter chemical composition over Europe: brake wear pollution. *Environment*
833 *International*, 109615.

834 Via, M., Minguillón, M. C., Reche, C., Querol, X., & Alastuey, A. (2021). Increase in secondary organic aerosol
835 in an urban environment. *Atmospheric chemistry and physics*, 21(10), 8323-8339.

836 Via, M., Chen, G., Canonaco, F., Daellenbach, K. R., Chazeanu, B., Chebaicheb, H., Jiang, J., Keernik, H., Lin,
837 C., Marchand, N., et al.: Rolling vs. seasonal PMF: real-world multi-site and synthetic dataset comparison,
838 *Atmospheric measurement techniques*, 15, 5479–5495, 2022.

839 Viana, M., Kuhlbusch, T. A., Querol, X., Alastuey, A., Harrison, R. M., Hopke, P. K., ... & Hitzenberger, R.
840 (2008). Source apportionment of particulate matter in Europe: a review of methods and results. *Journal of aerosol*
841 *science*, 39(10), 827-849.

842 Yang, Y., Ruan, Z., Wang, X., Yang, Y., Mason, T. G., Lin, H., & Tian, L. (2019). Short-term and long-term
843 exposures to fine particulate matter constituents and health: A systematic review and meta-
844 analysis. *Environmental pollution*, 247, 874-882.

845 Zhang, Y., Albinet, A., Petit, J. E., Jacob, V., Chevrier, F., Gille, G., ... & Favez, O. (2020). Substantial brown
846 carbon emissions from wintertime residential wood burning over France. *Science of the Total Environment*, 743,
847 140752.

848 Zhang, Y., Ma, X., Tang, A., Fang, Y., Misselbrook, T., & Liu, X. (2023). Source Apportionment of Atmospheric
849 Ammonia at 16 Sites in China Using a Bayesian Isotope Mixing Model Based on $\delta^{15}\text{N-NH}_x$
850 Signatures. *Environmental Science & Technology*, 57(16), 6599-6608.

851 Zheng, Y., Xue, T., Zhao, H., & Lei, Y. (2022). Increasing life expectancy in China by achieving its 2025 air
852 quality target. *Environmental science and ecotechnology*, 12, 100203.

853 Figures

854 **Table 1. Models used in the current study and their priors on the G, F matrices.**

855

Model	G priors	F priors
BMF	None	None
BMF+HS	None	Regularised horseshoe
BAMF	Rusanen et al. (2024)	None
BAMF+HS	Rusanen et al. (2024)	Regularised horseshoe
BAMF-AR1	AR(1)	None
BAMF-AR1+HS	AR(1)	Regularised horseshoe
BAMF-GS	Rusanen et al. (2024)	None
PMF	None	None

CMB	Fixed a-priori.	None
CMB+HS	Fixed a-priori.	Regularised horseshoe

856

857

Table 2. Profile sparsity metrics for the truth of synthetic datasets.

858

Dataset	Factor	F Gini	% zeros	
Chemically-sparse synthetic toy dataset	Factor 1	0.67	75.0	
	Factor 2	0.67	75.0	
	Factor 3	0.5	25.0	
Chemically-sparse synthetic offline dataset	Dust	0.74	37.5	
	Traffic	0.86	12.5	
	Salt	0.78	37.5	
	Coarse biological	0.88	25.0	
Less chemically-sparse synthetic online ACSM datasets	HOA	Krakow	0.74	5.0
		Milan	0.67	0.0
		Paris	0.68	0.0
		Zurich	0.68	0.0
	BBOA	Krakow	0.47	1.2
		Milan	0.72	0.0
		Paris	0.74	0.0
		Zurich	0.58	0.0
	SOA _{bio}	Krakow	0.52	0.0
		Milan	0.50	0.0
		Paris	0.50	0.0

		Zurich	0.67	0.0
	SOA _{BB}	Krakow	0.55	0.0
		Milan	0.53	0.0
		Paris	0.53	0.0
		Zurich	0.73	0.0
	SOA _{TR}	Krakow	0.45	0.0
		Milan	0.42	0.0
		Paris	0.46	0.0
		Zurich	0.60	0.0

859

860 **Table 3. Toy experiment statistics of (a) Factorisation performance. (b) Comparison to truth. Green**
861 **sequential colorscales represent variables whose larger value leans to a better performance and the blue-**
862 **to-red divergent colorscales (centered at 1, in white) represent G/G_0 divergence with respect to 1. Red bars**
863 **in (a) depict deviations from the ideal 0 value.**

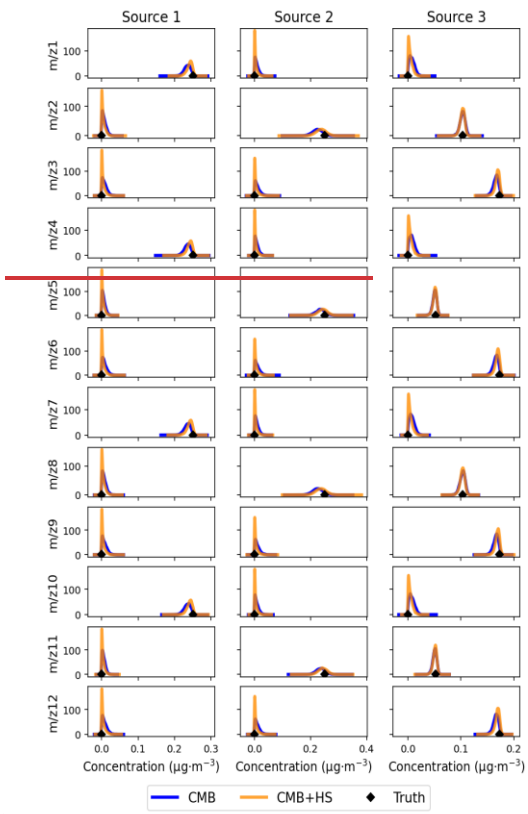
864

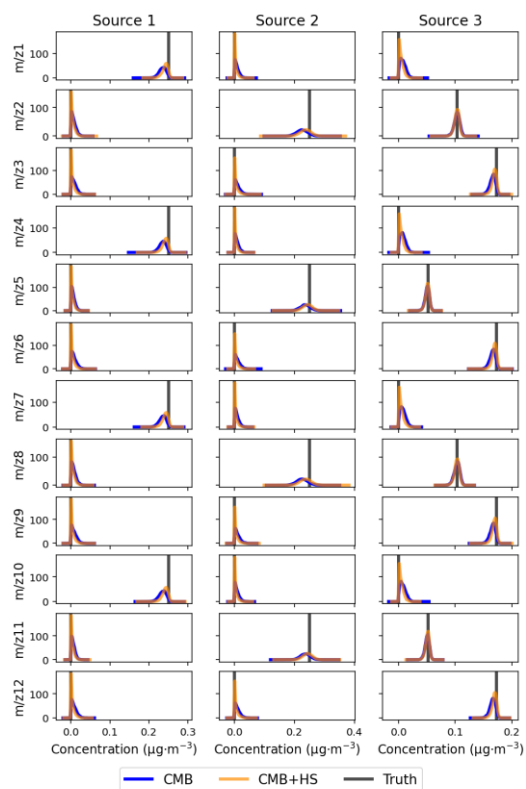
(a)

Model	Factorisation		
	R ²	Median(Z-X /sigma)	Max(Z-X /sigma)
CMB	0.9985	0.2542	0.5755
CMB+HS	0.9996	0.2648	0.4774
PMF	0.9979	0.2658	0.5847
BMF	0.9650	0.2125	1.2917
BMF+HS	0.9689	0.2107	1.2863
BAMF	0.9818	0.1222	0.7247
BAMF+HS	0.9820	0.1208	0.7180
BAMF-AR1	0.9806	0.0947	1.0257
BAMF-AR1+HS	0.9790	0.1171	1.0297
BMF-GS	0.9657	0.2024	1.3031
BAMF-GS	0.9818	0.1576	0.9082

(b)

Model	Sources	G				F		
		G/G ₀	R ²	ρ	R [†]	Gini	Gini ratio	Zeros sum
CMB	Source1	1.00	1.00	0.82	1.00	0.61	0.91	0.06
	Source2	1.00	1.00	0.82	1.00	0.60	0.90	0.08
	Source3	1.00	1.00	0.96	1.00	0.44	0.92	0.03
CMB+HS	Source1	1.00	1.00	0.82	1.00	0.63	0.95	0.03
	Source2	1.00	1.00	0.82	1.00	0.63	0.95	0.04
	Source3	1.00	1.00	0.96	1.00	0.47	0.96	0.02
PMF	Source1	1.00	0.96	0.82	0.95	0.35	0.52	0.36
	Source2	3.29	0.97	0.82	0.88	0.30	0.45	0.42
	Source3	0.65	0.74	0.79	0.81	0.31	0.64	0.2
BMF	Source1	1.08	0.87	0.82	0.76	0.25	0.37	0.48
	Source2	4.10	0.84	0.51	0.43	0.16	0.23	0.58
	Source3	0.60	0.46	0.79	0.80	0.21	0.44	0.25
BMF+HS	Source1	1.11	0.88	0.82	0.77	0.25	0.38	0.48
	Source2	3.92	0.85	0.82	0.50	0.15	0.23	0.57
	Source3	0.60	0.44	0.79	0.84	0.22	0.46	0.23
BAMF	Source1	1.66	0.98	0.82	0.78	0.27	0.41	0.46
	Source2	1.99	0.95	0.82	0.97	0.33	0.50	0.37
	Source3	0.54	0.50	0.96	1.00	0.38	0.79	0.08
BAMF+HS	Source1	1.96	0.98	0.82	0.76	0.27	0.40	0.47
	Source2	1.28	0.95	0.82	0.99	0.58	0.86	0.11
	Source3	0.51	0.48	0.96	1.00	0.44	0.93	0.02
BAMF-AR1	Source1	1.70	0.98	0.82	0.79	0.27	0.41	0.46
	Source2	3.05	0.92	0.82	0.89	0.37	0.55	0.36
	Source3	0.42	0.50	0.96	0.94	0.43	0.90	0.08
BAMF-AR1+HS	Source1	1.92	0.99	0.82	0.77	0.26	0.39	0.46
	Source2	2.58	0.89	0.82	0.90	0.48	0.72	0.36
	Source3	0.38	0.49	0.96	0.97	0.49	1.03	0.08
BMF-GS	Source1	0.88	0.92	0.82	0.63	0.21	0.31	0.52
	Source2	1.12	0.86	0.82	0.71	0.20	0.30	0.53
	Source3	1.02	0.29	0.79	0.91	0.22	0.46	0.22
BAMF-GS	Source1	0.89	0.94	0.82	0.66	0.21	0.32	0.53
	Source2	1.12	0.95	0.82	0.70	0.19	0.28	0.53
	Source3	1.02	0.36	0.79	0.90	0.22	0.46	0.22
BAMF-Lasso	Source1	1.76	0.98	0.82	0.76	0.27	0.40	0.47
	Source2	2.02	0.95	0.82	0.95	0.34	0.50	0.37
	Source3	0.49	0.47	0.96	1.00	0.41	0.86	0.05
BAMF-Spike-Slab	Source1	1.57	0.97	0.82	0.77	0.26	0.40	0.47
	Source2	1.78	0.95	0.82	0.99	0.34	0.52	0.34
	Source3	0.62	0.50	0.96	0.98	0.33	0.69	0.12

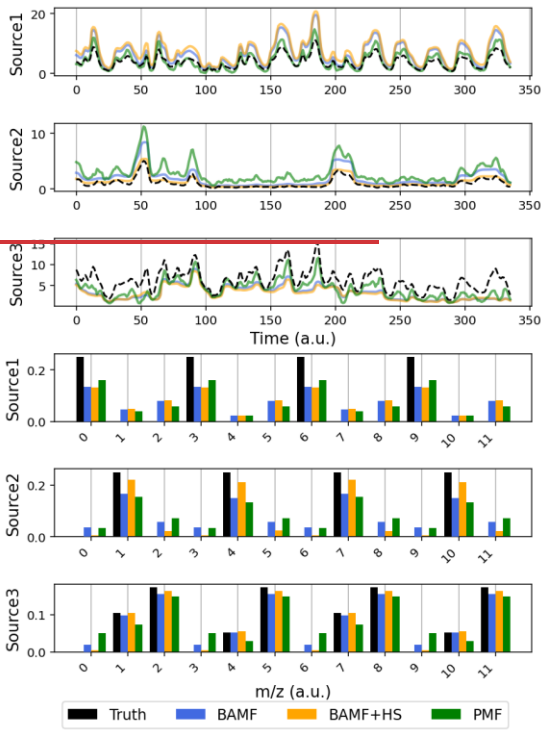




867

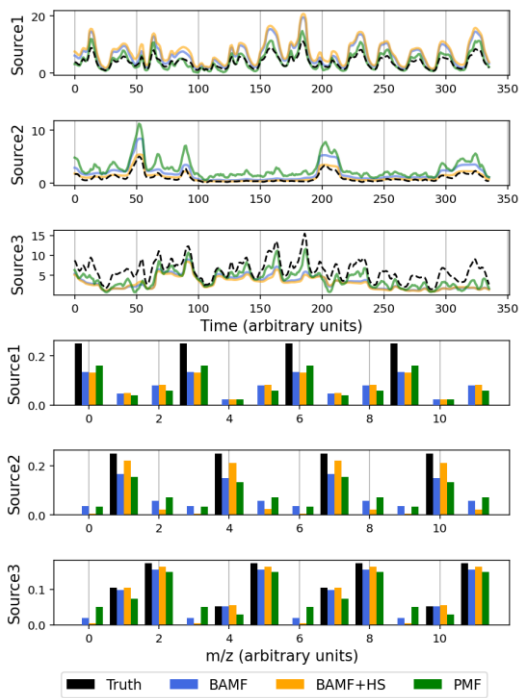
868 **Figure 1. Distributions for the mass concentrations of all measured variables (m/z) for both F-matrix-components**
 869 **distributions for CMB and CMB+HS (solid lines) compared to truth (markers).**

870



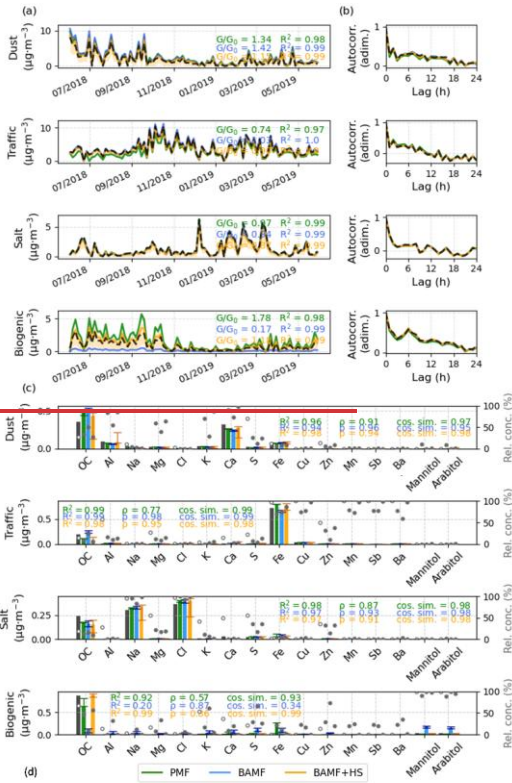
871

Formatted: English (United States)

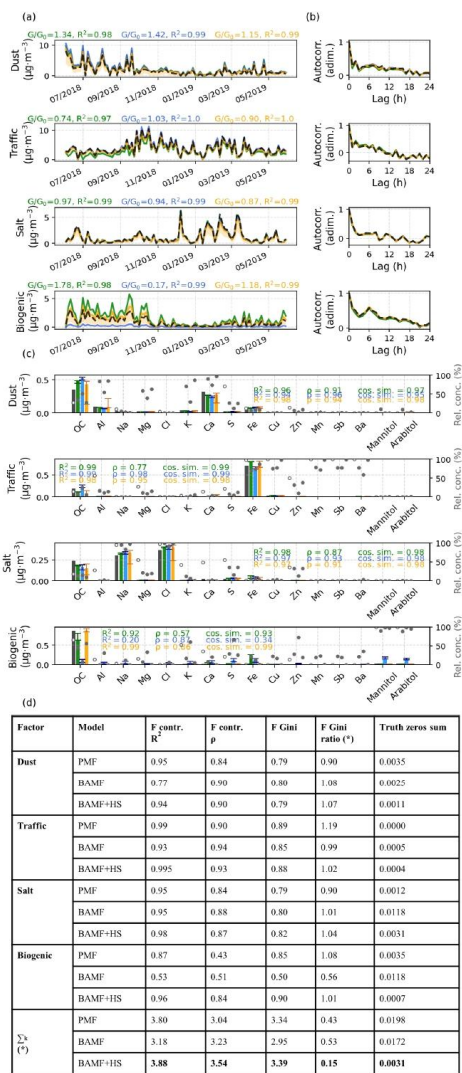


872

873 **Figure 2. Source apportionment results for the toy dataset obtained using PMF, BAMF, and BAMF+HS, compared**
 874 **against the true solution (black bars). (a) Factor time series. (b) Factor profiles.**



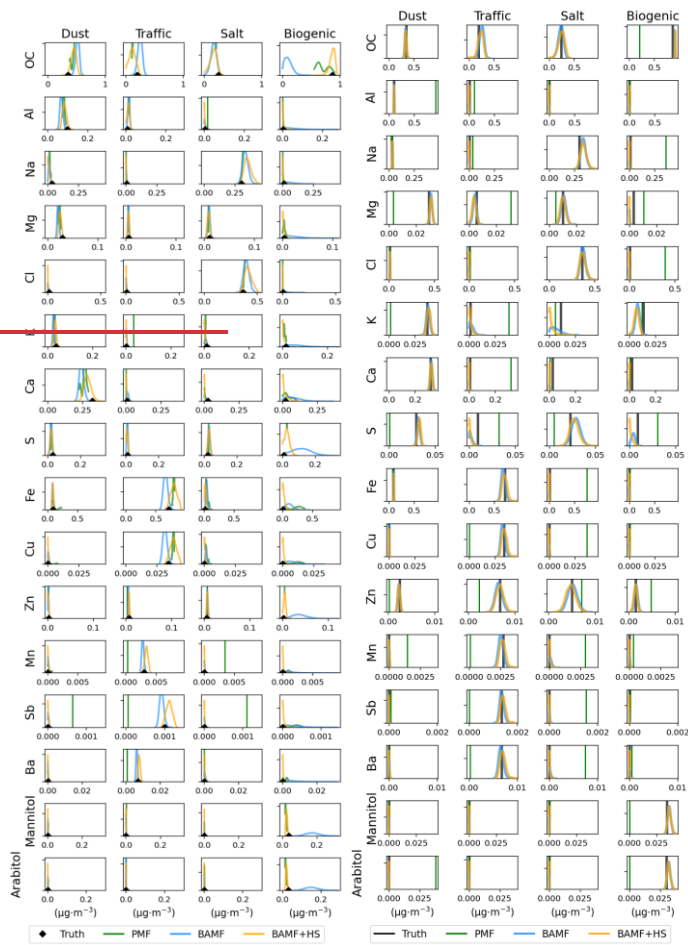
Factor	Model	F contr. R ²	F contr. p	F Gini	F Gini ratio (%)	Truth zeros sum
Dust	PMF	0.95	0.84	0.79	0.90	0.0035
	BAMF	0.77	0.90	0.80	1.08	0.0025
	BAMF-HS	0.94	0.90	0.79	1.07	0.0011
Traffic	PMF	0.99	0.90	0.89	1.19	0.0090
	BAMF	0.93	0.94	0.85	0.99	0.0005
	BAMF-HS	0.995	0.93	0.88	1.02	0.0004
Salt	PMF	0.95	0.81	0.79	0.90	0.0012
	BAMF	0.95	0.88	0.80	1.01	0.0118
	BAMF-HS	0.98	0.87	0.82	1.01	0.0051
Biogenic	PMF	0.87	0.43	0.85	1.08	0.0035
	BAMF	0.53	0.51	0.50	0.56	0.0118
	BAMF-HS	0.96	0.84	0.90	1.01	0.0007
Σ _i (°)	PMF	3.80	3.04	3.34	0.43	0.0198
	BAMF	3.18	3.23	2.95	0.53	0.0172
	BAMF-HS	3.88	3.54	3.39	0.15	0.0031



876

877 **Figure 3. Synthetic offline dataset source apportionment results for PMF, BAMF, and BAMF+HS models. (a) Time**
 878 **Series. (b) Autocorrelation. (c) Profiles. (d) Table with additional metrics for comparison to truth. Bold numbers reflect**
 879 **the highest value amongst models. F contr. represents here the percentage of each factor in to a given species. The sum**
 880 **row reflects the overall performance of the model for all sources for each statistic metric except for the ones marked**
 881 **with (*), in which the difference to 1 in absolute value is summed up.**

882



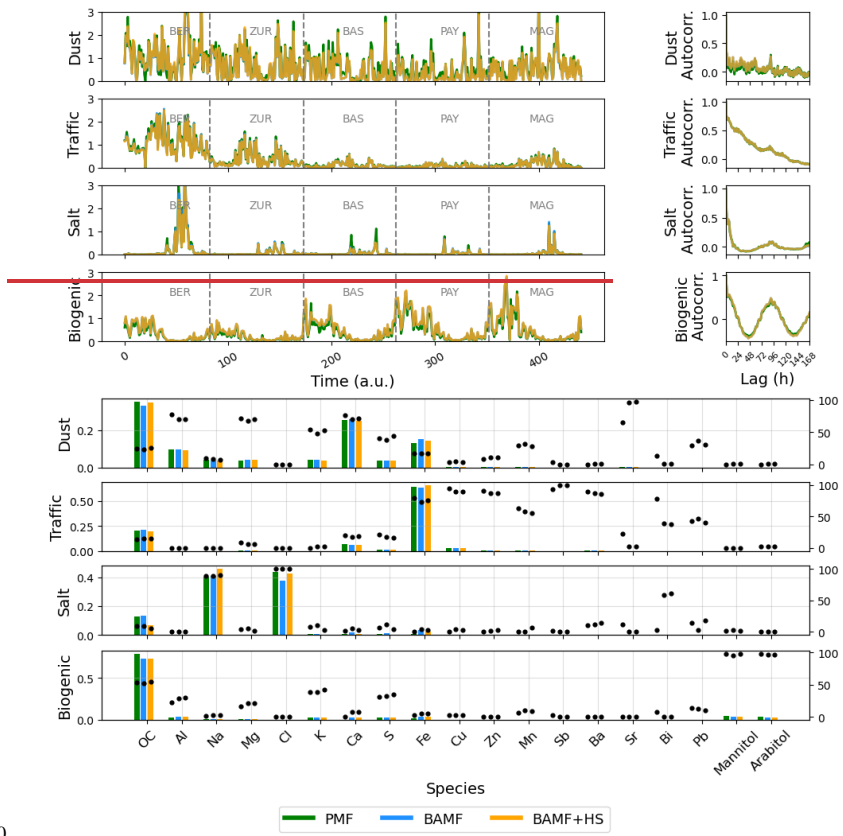
883

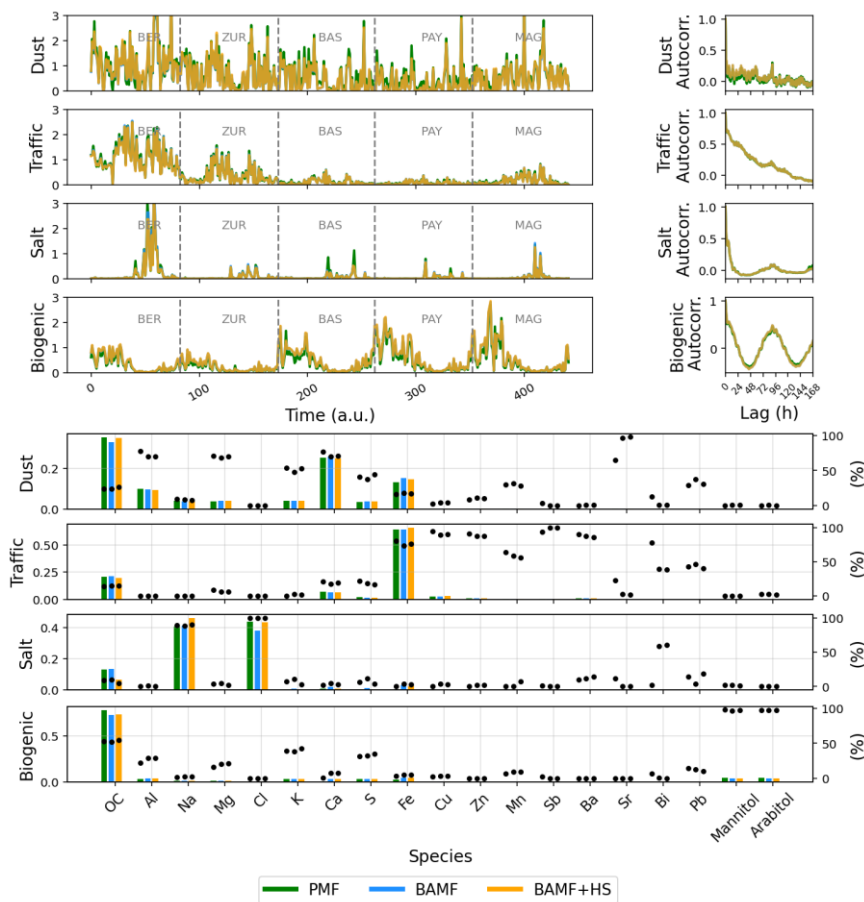
884

885 **Figure 4. Profile components distribution for PMF, BAME, BAME+HS (solid colored lines) in comparison**
886 **to the truth (markers/black lines) on the real-world filters dataset. Rows represent the species of the source**
887 **apportionment and columns represent sources.**

888

889





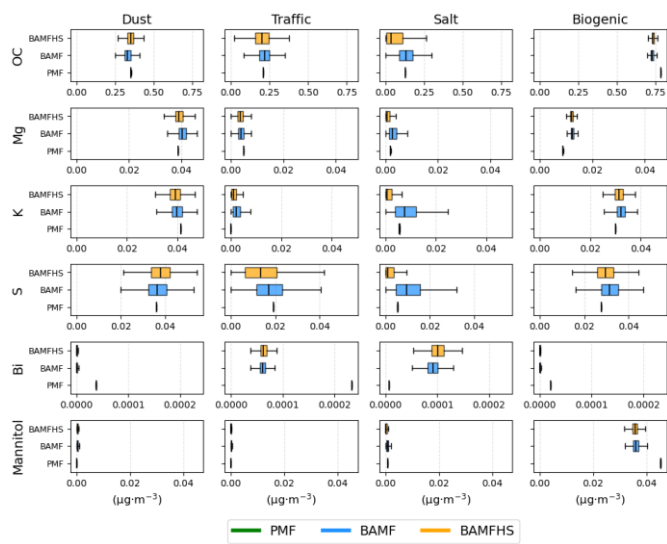
891
 892 **Figure 5. Comparison of PMF, BAMF, BAMF+HS for the real-world filters dataset. From left to right and**
 893 **top to bottom: time series, autocorrelation, and profile plots. The dots in the profiles (right axis) show the**
 894 **contribution of each species to the source.**

895 **Table 4. Offline real-world dataset reconstruction and sparsity statistics. Bold numbers reflect the highest**
 896 **value amongst models.**

Model	$R^2(Z, X)$	Median $ X-Z /\sigma$	Median $ X-Z /\sigma$	Factor	F Gini
PMF	0.68	0.77	10.52	Dust	0.77
				Traffic	0.87
				Salt	0.86
				Biogenic	0.87

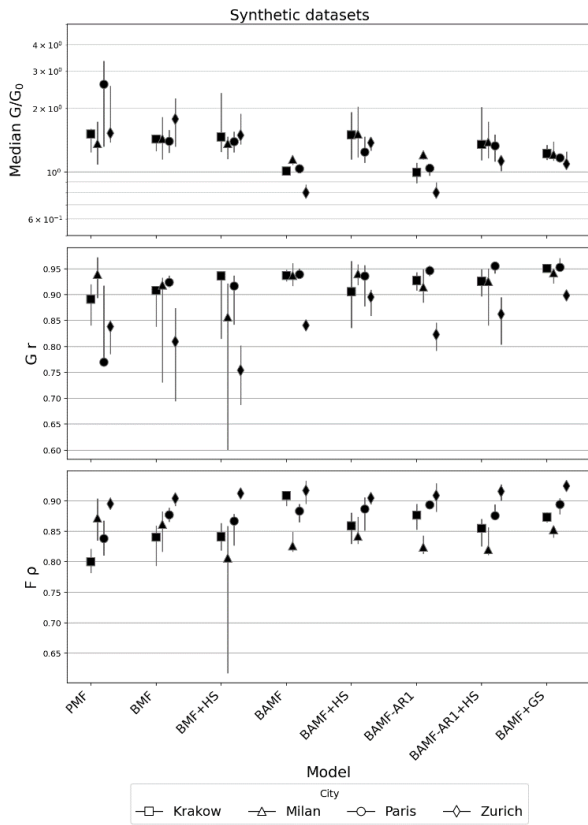
BAMF	0.67	0.75	11.13	Dust	0.76
				Traffic	0.87
				Salt	0.84
				Biogenic	0.83
BAMF+HS	0.67	0.75	11.12	Dust	0.77
				Traffic	0.87
				Salt	0.87
				Biogenic	0.83

897
898
899
900
901



902
903
904
905

Figure 6. Boxplot distributions of individual profile components derived from PMF, BAMF, and BAMF+HS analyses for the real-world filter dataset. A complete comparison of all profiles is presented in Figure S9.



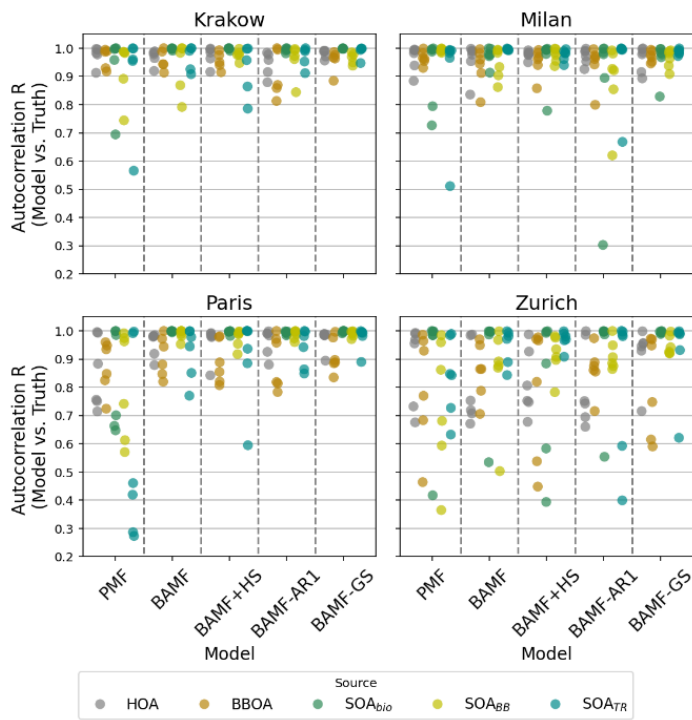
906

907

908

909

Figure 7. European cities synthetic datasets summary statistics; from top to bottom, median ratio time series with truth (G/G_0), Pearson correlation coefficient of G with truth ($G r$), Spearman correlation coefficient of F with truth ($F \rho$). The axis of the G/G_0 plot is in logarithmic scale.

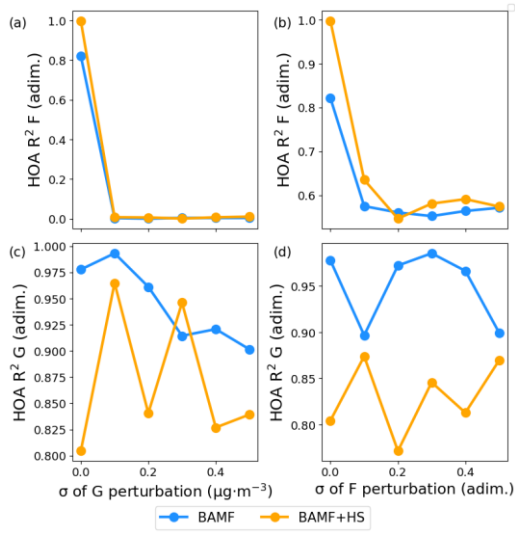


910

911 **Figure 8. Pearson correlation of the autocorrelations of model solutions with the truth for all factors and all cities.**

912

913



914
 915
 916
 917

Figure 9. Squared Pearson coefficient of F, G matrix with original truth F, G matrices of the BAMF, BAMF+HS models with the degrees of perturbation in F and G.